

The Impact of aerosol-ice nuclei-cloud interactions on a Typical Spring Dust-Precipitation Event in China

Jian Zhang^{1,2}, Chunhong Zhou^{2*}, Xiaoyu Shen^{2,3}, Hong Wang^{2,4}, Sunling Gong^{2,4,6,7}, Xiaoye Zhang^{5*}

¹ Key Laboratory for Aerosol-Cloud-Precipitation of China Meteorological Administration, Nanjing University of Information Science & Technology, Nanjing, Jiangsu, China

² Institute of Atmospheric Composition and Environmental Meteorology & Key Laboratory of Atmospheric Chemistry of CMA, Chinese Academy of Meteorological Sciences, Beijing, China

³ Key Laboratory of Urban Air Particulate Pollution Prevention and Control of the Ministry of Ecology and Environment, College of Environmental Science and Engineering, Nankai University, Tianjin, China

⁴ State Key Laboratory of Severe Weather, Chinese Academy of Meteorological Sciences, Beijing, China

⁵ Laboratory of Climate Change Mitigation and Carbon Neutrality, Henan University, Zhengzhou, Henan, China

⁶ National Observation and Research Station of Coastal Ecological Environments in Macao, Macao Environmental Research Institute, Macau University of Science and Technology, Macao, China

⁷ Research Institute for Pollution and Carbon Mitigation Assessment, Tianfu Yongxing Laboratory, Chengdu, Sichuan, China

* Corresponding authors.

E-mail addresses: zhouch@cma.gov.cn (Chunhong Zhou) and xiaoye@cma.gov.cn (Xiaoye Zhang)

Abstract

To investigate the impact of ice nuclei (IN) activated by dust aerosols on precipitation over China, a new mechanism for online aerosol activation of IN has been embedded in the Global/Regional Assimilation and Prediction System-China Meteorological Administration Unified Atmospheric Chemistry Environment (GRAPES/CUACE). The original temperature-dependent IN nucleation scheme in the Double-Moment 6-Class (WDM6) has been improved by the new online aerosol-IN nucleation scheme, which is used to examine the effects of these processes during a typical dust-affected precipitation event in East Asia. Compared with the systematic underestimation in the original WDM6, the peak values of nucleated INs reach 10^{-4} L^{-1} with the improved scheme, which is closer to observations. Above 7 km, dust suppresses both heterogeneous nucleation and deposition growth. Thus, the total

36 production rate of cloud ice drops to less than 24% of that in the control test T_CTL,
37 promoting snow formation and reducing the total ice-phase hydrometeor content to 70–
38 85% of T_CTL. Between 4 and 7 km, dust enhances heterogeneous nucleation of cloud
39 ice but suppresses deposition growth, thereby reducing the total ice-phase hydrometeor
40 content to 85–91% of T_CTL. Below 4 km, dust suppresses the conversion of water
41 vapour to cloud water, thereby reducing the liquid-phase hydrometeor content to 90–
42 95% of T_CTL. Dust can also modify the precipitation distribution, bringing it closer
43 to observations. It suppresses precipitation near dust source areas, where mean
44 precipitation decreases by about 4.5 mm, while the downstream event-mean
45 precipitation increases by about 1.1 mm.

46

47 Keywords: aerosol–IN–cloud–precipitation interactions; dust-precipitation event;
48 online aerosol–IN nucleation scheme; CUACE

49 **1 Introduction**

50 The formation of cloud ice is one of the key processes in ice-phase precipitation,
51 and ice nuclei (IN) associated with aerosols play a crucial role in the development of
52 cloud ice, particularly in mid- to high-latitude areas and in the upper troposphere (Li et
53 al., 2022; Chen et al., 2023; Knopf and Alpert, 2023). This is because homogeneous
54 nucleation without IN occurs only below $-40\text{ }^{\circ}\text{C}$, which is relatively rare in natural
55 atmospheric environments (Eastwood et al., 2008; Herbert et al., 2015; Kumar et al.,
56 2020; Che et al., 2021). In contrast, heterogeneous nucleation mediated by IN can occur
57 under ice-supersaturated conditions at much higher temperatures, making it the
58 dominant pathway for cloud ice formation.

59 Aerosols can serve as IN, participating in cloud formation, altering cloud
60 microphysical properties and lifetimes, and thereby affecting precipitation (Albrecht,
61 1989; Andreae and Crutzen, 1997). Among different species, mineral dust is recognized
62 as one of the primary sources of atmospheric IN (Khain et al., 2000; Nenes et al., 2014;
63 Tobo et al., 2019). Dust particles have unique surface structures that facilitate the
64 adsorption and binding of water molecules, promoting the formation of cloud ice
65 (Possner et al., 2017; Stevens et al., 2018). Stith et al. (2009) and DeMott et al. (2015)
66 have found a strong correlation between IN number concentration and aerosols with
67 diameters larger than $0.5\text{ }\mu\text{m}$, with mineral dust accounting for 33-50% of the total IN.
68 Jiang et al. (2016) combined IN measurements during dust conditions at multiple sites
69 in China, including Xinjiang (Jiang et al., 2016), Mt. Huangshan (Jiang et al., 2015),
70 and Nanjing (Yang et al., 2013), and found that IN concentrations were significantly
71 higher than those under non-dust conditions. Tobo et al. (2020) observed that IN
72 concentrations increased markedly during dust events in Tokyo when temperatures
73 exceeded $-25\text{ }^{\circ}\text{C}$. In addition, the increased solubility of aged dust aerosol enhances its
74 ability to act as cloud condensation nuclei (CCN), thereby further influencing
75 precipitation (Trochkin et al., 2003).

76 Compared with the relatively well-understood impacts of aerosols as CCN, the
77 role of dust as IN is considerably more complex and remains poorly understood, with
78 substantial uncertainties (Kaufman et al., 2002; Eastwood et al., 2008; Pan et al., 2017;

79 Possner et al., 2017). Based on the chemistry (WRF-Chem) model and multiple
80 observational and reanalysis data, Wang et al. (2024) found that dust aerosols can
81 suppress light precipitation by increasing atmospheric stability and inhibiting the
82 conversion of cloud droplets into raindrops. In contrast, Naeger (2018) found that dust
83 could enhance precipitation over Florida based on multi-sensor satellite observations
84 and field campaigns. More recently, Hu et al. (2023) demonstrated that the impact of
85 springtime dust on precipitation is strongly modulated by the presence of other aerosol
86 types. Liu et al. (2024) analysed the spatiotemporal patterns and trends of dust aerosols
87 and precipitation and found that increased dust suppresses precipitation over source
88 regions such as the Gobi and Taklamakan deserts, but enhances precipitation in
89 downwind areas such as northern China. Overall, because multiple factors influence
90 precipitation beyond aerosols, it remains challenging to quantify the impact of dust on
91 precipitation from observations alone (Zhou et al., 2016; Stier et al., 2024), highlighting
92 the need for process-oriented numerical modelling studies with physically based
93 aerosol–ice nucleation parameterisations.

94 A numerical model is a crucial approach for numerically studying the impact of
95 dust on precipitation. In early cloud microphysics schemes, the ice nucleation scheme
96 did not account for aerosols, with IN concentrations typically expressed as functions of
97 temperature or supersaturation (DeMott et al., 2010). Moreover, many cloud ice
98 microphysical schemes were single-moment, which only simulated the mass mixing
99 ratio of cloud ice. Such single-moment schemes often led to large biases in cloud ice
100 mass concentrations (Molthan and Colle, 2012; Igel et al., 2015). In contrast, double-
101 moment ice schemes, which simulate both cloud ice mass and number concentrations,
102 outperform single-moment schemes in simulating structure, life cycle, cloud coverage,
103 precipitation, and microphysical properties (Pu and Lin, 2015; Zhao et al., 2021). The
104 double-moment ice schemes can provide more stable and improved precipitation
105 simulations (Kang et al., 2018; Shen et al., 2022; Shen et al., 2024). Mascioli et al.
106 (2021) used the Thompson aerosol-aware microphysics scheme, incorporating the IN
107 nucleation scheme of DeMott et al. (2010), to study the sensitivity of precipitation to

108 different prescribed dust aerosol concentrations. Park and Lim (2023) developed the
109 revised Weather Research and Forecasting Double-Moment 6-class (WDM6) scheme
110 by implementing prognostic cloud ice number concentrations. The excess generation of
111 cloud ice mixing ratio is considerably alleviated. However, these studies did not
112 establish an explicit quantitative relationship between online aerosols and IN. Su and
113 Fung (2018a) implemented the simplified Goddard Chemistry Aerosol Radiation and
114 Transport aerosol model (GOCART) together with Shao's dust emission scheme (Kang
115 et al., 2011; Shao et al., 2011) in WRF/Chem and incorporated the online IN nucleation
116 scheme of DeMott et al. (2015) for producing real-time IN into the double-moment
117 Thompson–Eidhammer microphysics scheme. They analysed the impact of dust on
118 radiative forcing and temperature in East Asia, but only the sensitive impacts on
119 precipitation rates in March and April 2012 (Su and Fung, 2018b). The spring of 2012
120 was not a typical dust season; most dust storms concentrated in Mongolia. Therefore,
121 the microphysical pathways through which dust affects precipitation during typical dust
122 events remain insufficiently studied. In this study, we focus on a representative spring
123 dust precipitation event and explicitly examine the cloud microphysical processes
124 associated with dust-induced heterogeneous ice nucleation, together with direct
125 comparisons to precipitation observations in the Global/Regional Assimilation and
126 PrEdiction System, China Meteorological Administration (CMA) Unified Atmospheric
127 Chemistry Environment (GRAPES/CUACE) model. GRAPES/CUACE provides
128 online sectional aerosol concentrations with multi-chemical composition information
129 (Wang et al., 2010; Zhou et al., 2012). Zhou et al. (2016) introduced an online aerosol–
130 CCN–cloud interaction scheme into the system, allowing the model to simulate real-
131 time CCN activation and their influence on precipitation. However, in the
132 GRAPES/CUACE microphysics scheme WDM6, IN is a function of temperature only,
133 and cloud ice is represented by a single-moment scheme only for the mass mixing ratio
134 (Hong et al., 2004; Zhang et al., 2022).

135 To address these limitations, this study implements a double-moment cloud ice
136 scheme and incorporates an online aerosol–IN nucleation scheme to explicitly represent

137 heterogeneous processes. Using this improved framework, we then investigate the
138 impact of dust on precipitation through a typical dust-affected precipitation event in
139 East Asia. This paper is organised as follows: Section 2 introduces the model
140 configuration, cloud microphysical processes, the online aerosol–IN nucleation scheme,
141 the study region, and the observational datasets. Section 3 presents the evaluation of the
142 improved model's simulation performance and discusses the effects of dust on
143 precipitation. Section 4 summarises the main conclusions of the study.

144 **2 Model description and methodology**

145 **2.1 GRAPES/CUACE**

146 The GRAPES is a fully compressible, non-hydrostatic numerical weather model
147 that employs a semi-implicit, semi-Lagrangian discretisation scheme (Chen et al., 2008;
148 Xu et al., 2008; Zhang and Shen, 2008; Wang et al., 2022). Its physical parameterisation
149 packages include cumulus convection, single-moment cloud microphysics, radiation,
150 land surface processes, and boundary layer processes. CUACE is a regional chemical
151 weather forecasting system developed by Gong and Zhang (2008), coupled online with
152 GRAPES (Wang et al., 2010). It is capable of simulating seven aerosol species of sulfate,
153 nitrate, ammonium, black carbon, organic carbon, sea salt, and dust (Zhou et al., 2008,
154 2012; Wang et al., 2015). The sectional dust emission scheme is by Marticorena and
155 Bergametti (1995) and Alfaro and Gomes (2001), which has been improved by surface
156 dust flux observations and desertification in East Asia (Gong et al., 2003), and a new
157 desertification map and soil texture samples from Chinese deserts (Zhou et al., 2019;
158 Zhou et al., 2024). The aerosol size spectra have been divided into 12 size bins with a
159 radius range of 0.005–0.01, 0.01–0.02, 0.02–0.04, 0.04–0.08, 0.08–0.16, 0.16–0.32,
160 0.32–0.64, 0.64–1.28, 1.28–2.56, 2.56–5.12, 5.12–10.24, and 10.24–20.48 μm .
161 GRAPES/CUACE has a horizontal resolution of 0.15° and 31 vertical levels extending
162 to approximately 28.6 km.

163 **2.2 WDM6 microphysics scheme**

164 In this study, we select the WDM6 microphysics scheme in GRAPES to simulate
165 precipitation (Hong et al., 2004; Zhang et al., 2022). The WDM6 scheme simulates the

166 mass mixing ratio of water vapour (Q_v), as well as the mass and number concentrations
167 of cloud water (Q_c) and rainwater (Q_r) in warm clouds. For icy clouds, it includes the
168 mass mixing ratios of cloud ice (Q_i), snow (Q_s), and graupel (Q_g). A double-moment
169 cloud ice scheme by Park and Lim (2023) is incorporated into the WDM6 scheme,
170 enabling explicit prediction of cloud ice number concentration. A sectional CCN-
171 activated scheme has been introduced in WDM6 in GRAPES/CUACE, connecting the
172 multi-component, multi-section aerosols from CUACE to the WDM6 microphysics and
173 the sub-grid convective parameterisation scheme via newly activated CCN at each time
174 step (Zhou et al., 2016).

175 **2.3 Online aerosol-IN nucleation scheme**

176 In the original WDM6 scheme, when the temperature is below 0°C , the increase
177 in cloud ice mass concentration arises from two processes: heterogeneous nucleation
178 (Pigen) and deposition–sublimation of cloud ice (Pidep, when positive). Both consume
179 water vapour to form ice clouds. The abbreviations for the remaining cloud
180 microphysical processes are listed in Table 2. The IN concentration, N_{ice} (m^{-3}), is
181 calculated by a classical ice nuclei nucleation scheme, which is an empirical function
182 of temperature and does not account for the influence of atmospheric aerosols (Hong et
183 al., 2004):

$$N_{ice} = 10^3 e^{0.1(T_0 - T_k)} \quad (1)$$

184 Where, T_k is atmospheric temperature, T_0 is the freezing point (273.15 K).

185 This study implements an online aerosol-IN nucleation scheme in
186 GRAPES/CUACE that accounts for heterogeneous ice nucleation processes influenced
187 by atmospheric aerosols. Heterogeneous nucleation mechanisms are generally
188 classified into immersion freezing, condensation freezing, deposition nucleation, and
189 contact freezing (Hiranuma et al., 2015; Ilotoviz et al., 2016; Lee et al., 2017). Among
190 these mechanisms, immersion freezing, condensation freezing, and deposition
191 nucleation are selected, as they are relatively well developed. This selection is based on
192 the fact that dust aerosols primarily affect ice nucleation at temperatures below 258.15
193 K through these three mechanisms (Cantrell et al., 2013; Patnaude et al., 2025), whereas

194 the efficiency of contact freezing by dust particles is relatively low (Niehaus et al.,
195 2014).

196 Immersion freezing is a heterogeneous ice nucleation process with the existence
197 of liquid drops at temperatures between 233.15 K and 273.15 K, in which an ice nucleus
198 is immersed in a supercooled droplet, thereby triggering freezing into an ice crystal
199 (Boose et al., 2016). Immersion freezing consumes water vapour to form cloud ice. The
200 initial size of the ice crystal is influenced by the size of the liquid droplet (Fan et al.,
201 2014; Gibbons et al., 2018), therefore the cloud ice formation through this mechanism
202 is relatively easier compared to other nucleation mechanisms. The selected DeMott et
203 al. (2015), immersion-freezing nucleation scheme here is developed by DeMott et al.
204 (2015) and is based on continuous-flow diffusion-chamber measurements. The number
205 concentration of ice nuclei, N_{icenui} (m^{-3}), activated via immersion freezing is given by:

$$N_{icenui} = 3 * n_{aer,0.5}^{1.25} * e^{(0.46*(273.16-T_k)-11.6)} \quad (2)$$

206 Where, $n_{aer,0.5}^{1.25}$ is the number concentration of insoluble aerosol particles with
207 diameters exceeding 0.5 μm , such as dust, black carbon and part of organic carbon.

208 Deposition and condensation freezing are both heterogeneous ice nucleation
209 processes that occur at temperatures between 248.15 and 258.15 K (Chen et al., 2019).
210 In condensation freezing, water vapour first condenses on the surface of IN and
211 subsequently freezes to form an ice crystal, while in deposition nucleation, water vapour
212 directly deposits onto the IN surface (Kanji et al., 2017). The ice formation through
213 these two pathways is generally harder than that through immersion freezing (DeMott
214 et al., 2015). The parameterisation used here follows the formulation of Chen et al.
215 (2019). In Jiang et al. (2016), the ice-nucleating ability of dust aerosols was derived
216 from measurements conducted at several sites in China (Yang et al., 2013; Jiang et al.,
217 2015; Jiang et al., 2016), using a static vacuum vapour diffusion chamber based on the
218 FRIDGE (Frankfurt Ice Nuclei Deposition Freezing Experiment) design. Chen et al.
219 (2019) further refined the parameterisation to explicitly represent deposition and
220 condensation freezing processes within a specified temperature range. The number
221 concentration of ice nuclei produced by deposition and condensation freezing, $N_{icenuid}$

222 (m^{-3}), is calculated as follows:

$$\begin{aligned} \text{Nicenud} = & 5.7 * 10^{-7} n_{\text{aer},0.5}^{0.018(273.16-Tk)-0.007S_i+0.342} \quad (3) \\ & * (273.16 - Tk)^{3.745} * S_i^{1.31} \end{aligned}$$

223 Where, S_i is supersaturation with respect to ice.

224 WDM6 uses the formula $\rho q_{I0}(\text{kg m}^{-3}) = 4.92 \times 10^{-11} N_{\text{ice}}^{1.33}$ and $\text{Pigen}(\text{kg}$
225 $\text{kg}^{-1} \text{s}^{-1}) = \frac{(q_{I0}-q_I)}{\Delta t}$ to calculate newly nucleation of ice. Where, ρ denotes the newly-
226 formed air density, and q_{I0} is the predicted ice mixing ratio (kg kg^{-1}). Δt is the
227 integration time step. Production rate for heterogeneous nucleation is calculated as the
228 difference between q_{I0} and the current ice mixing ratio (q_I). However, it does not
229 account for the influence of nucleated IN size or the specific characteristics of different
230 heterogeneous ice nucleation mechanisms on ice crystal development.

231 Here, the mass production rate of cloud ice newly nucleated is calculated as
232 follows:

$$\begin{aligned} \text{Pinud} &= \frac{4}{3} \pi \frac{\rho_i}{\rho_a} (r_{\text{df}}^3 N_{\text{icenuud}}) / \Delta t \quad (4) \\ \text{Pinui} &= \frac{4}{3} \pi \frac{\rho_i}{\rho_a} (r_{\text{if}}^3 N_{\text{icenui}}) / \Delta t \end{aligned}$$

233 Where, Pinud ($\text{kg kg}^{-1} \text{s}^{-1}$) is the mass production rate for deposition/condensation
234 freezing, Pinui ($\text{kg kg}^{-1} \text{s}^{-1}$) is for immersion freezing. Pinud depletes water vapour to
235 form cloud ice, while Pinui depletes cloud water to form cloud ice. ρ_i is 500 kg m^{-3}
236 (Park and Lim, 2023). r_{if} represents the initial radius of cloud ice formed via
237 immersion freezing, while r_{df} represents the initial radius of cloud ice formed through
238 deposition and condensation freezing, respectively. Δt is the integration time step. In
239 the new online scheme, the production rate for nucleated IN number concentration
240 (N_{igen}) is the sum of N_{icenui} and N_{icenuud} .

241 The typical range of ice crystal radius in East Asia is about 10–100 μm (Chen et al.,
242 2021), droplet radius range is about 1-30 μm (Um et al., 2018; Yang et al., 2021).
243 Considering ice crystals generally grow from smaller particles and the radius of initial
244 ice crystal size are often smaller than observed values, and with reference to the bin
245 sizes of aerosol particles in CUACE (Um et al., 2018; Chen et al., 2021; Yang et al.,

246 2021), this study assumes the characteristic radius of ice crystals of r_{df} and r_{if} to be:

$$\begin{cases} r_{df} = 10 \mu\text{m} & (r_{aer} < 10 \mu\text{m}) \\ r_{df} = 30 \mu\text{m} & (r_{aer} > 10 \mu\text{m}) \\ r_{if} = 30 \mu\text{m} & (r_{aer} < 10 \mu\text{m}) \\ r_{if} = 50 \mu\text{m} & (r_{aer} > 10 \mu\text{m}) \end{cases} \quad (5)$$

247 Then, the original production rate for nucleation of ice from vapour Pigen in
248 WDM6 is replaced by the Pinud and Pinui described above.

249 **2.4 Case description and test design**

250 **The typical dust-affected precipitation event**

251 The typical dust-affected precipitation event spans from 00:00 UTC on 9 April to
252 00:00 UTC on 15 April 2018 and includes two dust storm events in East Asia. One is
253 from 9 to 11 April, originating in Mongolia and affecting northern China. Numerous
254 dust storm phenomena are observed in Mongolia, while blowing and floating dust
255 phenomena are reported in central and western Inner Mongolia, central Gansu, Ningxia,
256 northern Shaanxi, most parts of Shanxi, southern Hebei, northern Henan, and western
257 Shandong in China (see Fig. S1 for locations). Another event is from 13 to 14 April. It
258 also gains with widespread dust storms in Mongolia and central Inner Mongolia, and
259 with blowing or floating dust observed in central Inner Mongolia, northern Shanxi,
260 Beijing, Tianjin, and northern Hebei in China. Between the two dust storm events, the
261 precipitation occurred from west to east, covering most of northern China extending to
262 the Yangtze River area, from 00:00 UTC on 12 April to 00:00 UTC on 15 April,
263 concentrated in Shaanxi, Henan, southern Hebei, and along the Yangtze River in
264 Sichuan, Hubei, Anhui, and the Jiangsu-Zhejiang-Shanghai area.

265 Figure 1a presents the dust-affected areas by dust phenomenon from
266 Meteorological stations and PM_{10} from the National Environmental Monitoring
267 Network of the Ministry of Environmental Protection. Based on the distribution of dust
268 in this event, the domain bounded by 90-135 °E and 20-54 °N is defined as the major
269 dust-affected area (DA, region 1 in Figure 1). Together with the real precipitation
270 distribution (Fig. 5a), the domain bounded by 103°–130.5°E and 27.5°–50°N is defined
271 as the dust-affected precipitation (DP) area (DPA, region 2 in Figure 1). The whole

272 model domain covers 70° – 145° E and 15° – 64.5° N, containing the DA and DPA. To
273 investigate the impact of dust on precipitation in regions distant from the dust source in
274 Section 3.3, we calculate horizontal hydrometeor fluxes across 116° E (33° – 50° N) and
275 33° N (103° – 116° E) during 12:00 UTC on 12 April to 18:00 UTC on 13 April (Fig. 6).
276 The area bounded by 103° – 116° E and 33° – 50° N is defined as the near-dust-source area
277 (NDSA, region 3 in Figure 1).

278 GRAPES/CUACE successfully reproduces both the spatial distribution and
279 intensity of the dust events (Fig. 1b). Considering that many radar observations and
280 model studies have indicated that dust mainly participates in heterogeneous ice
281 nucleation as ice nuclei within the mid-tropospheric layer ($-20 - 0^{\circ}$ C) (Haarig et al.,
282 2019; He et al., 2021; He et al., 2023), which corresponds to altitudes between 4 and 7
283 km in the present case, Fig. 1c shows the simulated dust concentration within this layer.

284 **Test design**

285 As shown in Table 1, two tests are designed. The first test uses the online aerosol–
286 CCN–cloud interaction scheme from Zhou et al. (2016), denoted as T_CTL. Based on
287 T_CTL, the second test adds the online aerosol-IN nucleation scheme described in
288 Section 2.3, denoted as T_IN.

289 The successive integration is divided into several three-day intervals, with a warm
290 restart between them. It starts at 00:00 UTC on April 5, 2018, with 6 days spinning up
291 for tracers in CUACE. As simulation time increases, integration errors tend to
292 accumulate (Zhang et al., 2019), and to minimise the influence of initial conditions on
293 precipitation, the simulations in this study were divided into several time segments: 5–
294 8 April, 8–11 April, 11–14 April, and 13–16 April. Among these, the simulation results
295 for 13 April were taken from the 11–14 April experiment to minimise the influence of
296 initial conditions on precipitation development. Except for water vapour, all initial
297 hydrometeor values are zero for each run. The model outputs 1-hourly precipitation
298 data. To compare with the observed 6-hourly precipitation, the model outputs are
299 temporally interpolated to the observation timestamps.

300 The initial and boundary meteorological conditions for GRAPES/CUACE are from

301 the Final Operational Global Analysis data produced jointly by the National Centers for
 302 Environmental Prediction (NCEP) and the National Center for Atmospheric Research
 303 (NCAR) at a temporal resolution of 6 hours and a spatial resolution of 0.25°. The
 304 anthropogenic emissions are from the Multi-resolution Emission Inventory for China
 305 (Li et al., 2017).

306 **2.5 Data and evaluation methodology**

307 The initial and boundary meteorological conditions for GRAPES/CUACE are
 308 obtained from the NCEP/NCAR Final Operational Global Analysis (FNL) data, with a
 309 temporal resolution of 6 hours and a spatial resolution of 0.25°. Dust observations are
 310 obtained from two sources: weather phenomena from the CMA surface meteorological
 311 observation network with a 3-hour temporal resolution, and PM₁₀ and PM_{2.5}
 312 concentration data from the national environmental monitoring network of the Ministry
 313 of Ecology and Environment of China with a 1-hour temporal resolution. 6-hour rainfall
 314 data are also from the CMA surface meteorological observation network. As there are
 315 more than 2,000 precipitation stations in DA, only 63 level-1 and level-2 stations are
 316 selected for evaluation, of which 43 are in DPA to avoid overfitting in the model outputs.
 317 Due to the complex sources of PM₁₀ and considering the relatively long atmospheric
 318 residence time of dust, we select precipitation stations where the PM_{2.5}/ PM₁₀ ratio is
 319 less than 0.6 within 24 hours prior to the precipitation event as representative of dust-
 320 influenced precipitation (DP) stations (Wang and Yan, 2007; Filonchyk et al., 2019).

321 Model performance is evaluated using mean absolute error (MAE), root mean
 322 square error (RMSE), and symmetric mean absolute percentage error (sMAPE)
 323 (Shcherbakov et al., 2013):

$$\begin{aligned}
 \text{MAE} &= \frac{\sum_{i=1}^n |r_{mi} - r_{oi}|}{n} & (8) \\
 \text{RMSE} &= \sqrt{\frac{\sum_{i=1}^n (r_{mi} - r_{oi})^2}{n}} \\
 \text{sMAPE} &= \frac{1}{n} \sum_{i=1}^n \frac{|r_{mi} - r_{oi}|}{|r_{mi}| + |r_{oi}|} \\
 \text{aMAPE} &= \frac{r_{mi} - r_{oi}}{|r_{mi}| + |r_{oi}|}
 \end{aligned}$$

324 where r_{mi} represents the simulated cumulative precipitation at station i , and r_{oi}
325 denotes the observed precipitation. For MAE, RMSE and sMAPE, values closer to 0
326 indicate better simulation performance. The aMAPE is used to evaluate whether the
327 simulated precipitation is overestimated or underestimated relative to observations.
328 When $aMAPE > 0$, the precipitation is overestimated; when $aMAPE < 0$, the
329 precipitation is underestimated.

330 The horizontal hydrometeor fluxes shown in Section 3.3 are calculated using a grid-
331 based mass transport formulation. For each model layer, the flux is computed as

$$F = \rho_{air} q_x V_n \Delta z \Delta s \quad (9)$$

332 where F is the hydrometeor flux (kg s^{-1}), ρ_{air} is the air density (kg m^{-3}), q_x is the
333 mass mixing ratio of the hydrometeor species (kg kg^{-1}), V_n is the wind component
334 normal to the cross section (m s^{-1}). Specifically, for the north–south cross section along
335 116°E ($33^\circ\text{--}50^\circ\text{N}$), V_n is taken as the zonal wind component; for the west–east cross
336 section along 33°N ($103^\circ\text{--}116^\circ\text{E}$), V_n is taken as the meridional wind component. Δz
337 is the layer thickness (m), and Δs is the horizontal grid spacing along the cross section
338 (m).

339 **3 Results**

340 **3.1 Ice nuclei**

341 During the DP event, the implemented online aerosol–IN nucleation scheme
342 enables dust aerosols to modify the nucleated IN number concentration. Figures 2a and
343 2b show the horizontal distribution of the maximum nucleated IN number concentration
344 between 4 and 7 km above ground level at DP stations during the time period from
345 00:00 UTC on 11 April to 00:00 UTC on 15 April 2018 for T_CTL and T_IN,
346 respectively. Figure 2c presents the vertical distribution of DP-event-averaged
347 production rate for Nigen for T_CTL (red line) and T_IN (blue line). Figure 2d presents
348 the vertical distribution of cloud ice mass production rate for heterogeneous ice
349 nucleation for T_CTL and T_IN. Based on the variation characteristics, the vertical
350 layer is divided into three parts: layer A, above 7 km (temperature below -18°C); layer
351 B, between 4 and 7 km (temperature approximately -18°C to -1.5°C); and layer C,

352 below 4 km (temperature approximately $-1.5\text{ }^{\circ}\text{C}$ to $18\text{ }^{\circ}\text{C}$).

353 The online aerosol-IN nucleation scheme can correct the systematic
354 underestimation of IN concentrations. The maximum nucleated IN number
355 concentrations in T_CTL can reach 10^2 L^{-1} in layer B during the DP event (Fig. 2a),
356 showing a relatively uniform horizontal pattern, which is much lower than observed IN
357 concentrations ($10^2\text{--}10^4\text{ L}^{-1}$) during East Asian dust events (Bi et al., 2019; Tobo et al.,
358 2019; Chen et al., 2021; Hu et al., 2023). For example, Chen et al. (2021) measured
359 immersion-mode INPs at Peking University Atmosphere Environment Monitoring
360 Station during spring 2018–2019 and found that dust periods increased INP
361 concentrations by approximately two orders of magnitude, reaching 10^2 L^{-1} between -
362 $15\text{ }^{\circ}\text{C}$ and $-28\text{ }^{\circ}\text{C}$. The DP-event-averaged production rate for nucleated IN number
363 concentration ranges $0.005\text{--}0.01\text{ L}^{-1}\text{ s}^{-1}$ in layer B (Fig. 2c). In T_CTL, the production
364 rate for nucleated IN number concentration increases with height (Fig. 2c), primarily
365 due to the temperature-dependent nature of the original WDM6 scheme. As a result,
366 cloud ice mass production rate due to heterogeneous ice nucleation peak near the $-40\text{ }^{\circ}\text{C}$
367 level (Fig. 2d). Above this layer, IN concentration continues to increase, but production
368 rate of heterogeneously nucleated cloud ice begins to decline due to limited water
369 vapour (Fig. 2d). In the real atmosphere, the number concentration of effective ice-
370 nucleating particles often reaches a maximum in the mid-troposphere rather than at the
371 highest altitudes (He et al., 2023), suggesting that the continuous increase of IN at
372 higher altitudes in T_CTL may inconsistent with typical observed.

373 In T_IN, the maximum nucleated IN number concentrations can reach 10^4 L^{-1} in
374 layer B during the DP event (Fig. 2b), closer to those observed or simulated in other
375 East Asian dust events (Bi et al., 2019; Tobo et al., 2019; Chen et al., 2021; Hu et al.,
376 2023). The DP-event-averaged production rate for nucleated IN number concentration
377 ranges from 0.2 to $3.7\text{ L}^{-1}\text{ s}^{-1}$ in layer B (Fig. 2c), and the cloud ice mass production rate
378 for heterogeneous ice nucleation also peaks in this layer, which is consistent with radar
379 observations and other modelling studies (Haarig et al., 2019; He et al., 2021; He et al.,
380 2023). As immersion freezing is the dominant heterogeneous nucleation mechanism

381 (DeMott et al., 2015; Hiranuma et al., 2015), this study compares the number
382 concentration of ice-nucleating particles activated by immersion freezing with those
383 activated by deposition and condensation freezing. The DP-event-averaged results
384 indicate that the activated IN number concentration from immersion freezing exceeds
385 that from deposition and condensation freezing by approximately 4–5 orders of
386 magnitude.

387 **3.2 Hydrometeors**

388 During the DP event, the introduction of the online aerosol-IN nucleation scheme
389 allows dust aerosols to alter the distribution of cloud hydrometeors. Figure 3 shows the
390 DP-event-averaged vertical distributions of hydrometeors in T_CTL and T_IN,
391 averaged over the dust–precipitation period (00 UTC 11 April–00 UTC 15 April 2018)
392 and over dust–precipitation stations, as well as their difference (T_IN - T_CTL), by
393 using budget analysis. Figure 4 shows the differences in production rates among
394 hydrometeors (T_IN - T_CTL). To further examine the thermodynamic conditions
395 responsible for the weakened production rate of cloud droplet activation from CCN in
396 T_IN in Figure 4, the vertical profiles of temperature and water vapour were analyzed,
397 averaged over the dust–precipitation stations in DPA and NDSA during the period when
398 the dust impact was most pronounced (18:00 UTC 11 April to 18:00 UTC 12 April)
399 (Figure 5).

400 **Cloud ice**

401 In layer A, when dust aerosols are considered, the IN number concentration
402 decreases in T_IN (Fig. 2c), resulting in cloud ice number concentrations in T_IN that
403 are approximately 5 L^{-1} lower than those in T_CTL, about 40% of T_CTL (Fig. 3d).
404 The cloud ice mass concentration is reduced to only 10% - 50% of T_CTL (Fig. 3a,
405 3b). Because the two primary processes contributing to cloud ice formation in this
406 layer—heterogeneous nucleation and deposition-sublimation of cloud ice—are both
407 suppressed (Fig. 4a), and the total production rate of cloud ice (Pigen+Pidep-Psaut-
408 Praci-Psaci-Pgaci) drops to less than 24% of that in T_CTL. On the one hand, the
409 nucleated IN number concentration decreases, weakening the Pigen in T_IN by 1–2

410 orders of magnitude relative to T_CTL. On the other hand, the reduction in cloud ice
411 number concentration allows ice crystals to grow more efficiently, with their effective
412 particle size generally reaching 98% - 135% of that in T_CTL. The combined effect of
413 these two factors ultimately limits the deposition of water vapour onto the ice crystals.
414 Consequently, Pidep decreases to 20%–50% of T_CTL, with the maximum suppression
415 occurring at approximately 7–8 km (Fig. 4a).

416 In layer B, cloud ice number concentrations in T_IN range from 7 to 10 L⁻¹,
417 approximately 120% of those in T_CTL. However, the cloud ice mass concentration in
418 T_IN is reduced to only 70%–90% of T_CTL. The effective diameters of cloud ice also
419 decrease to only 77%–97% of T_CTL, with occasional reductions exceeding 50%. This
420 reduction is mainly attributable to the combined effects of enhanced heterogeneous
421 nucleation and suppressed depositional growth, and the total production rate of cloud
422 ice drops to less than 82% of that in T_CTL. Dust aerosols provide additional ice nuclei,
423 leading to a substantial enhancement of heterogeneous nucleation in T_IN and the
424 formation of a much larger number of newly formed small ice crystals, with Pigen
425 exceeding that in T_CTL by more than two orders of magnitude. However, the increase
426 in cloud ice number concentration is accompanied by a reduction in individual particle
427 size, which limits the deposition of water vapour onto ice crystals. This effect is
428 combined with a decrease in relative humidity over dust precipitation stations in the
429 DPA (Fig. 5c), further inhibiting the deposition process. As a result, Pidep in T_IN is
430 reduced to about 30% of that in T_CTL, indicating that growth of cloud ice via
431 depositional processes is inhibited.

432 **Snow**

433 In layer A, the total snow production rate in T_IN increases to approximately 88%
434 -200% of that in T_CTL ($P_{sdep}+P_{aacw}+P_{saut}+P_{iacr}+P_{raci}+P_{saci}+P_{sacr}-P_{gaut}-P_{racs}$,
435 Fig. 4b), leading to an increase in snow mass concentration to 120%–200% of T_CTL
436 (Fig. 3a, 3b). This increase results from the combined effects of an enhanced production
437 rate for deposition-sublimation of snow (P_{sdep}) and weakened production rates for the
438 aggregation of cloud ice to snow (P_{saut}) and the accretion of cloud ice by snow (P_{saci}).

439 The Psdep can reach approximately 2–5 times that in T_CTL (Fig. 4b). In WDM6, the
440 deposition growth of ice-phase hydrometeors is constrained by the available water
441 vapour, with cloud ice deposition given priority and snow deposition consuming the
442 remaining vapour. Because Pidep is reduced to about 20%–50% of that in T_CTL, more
443 water vapour is allocated to snow deposition, Psdep is then enhanced. Meanwhile, as
444 cloud ice reduces, Psaut and Psaci are weakened in T_IN, with both processes reduced
445 to approximately 40%–60% of their values in T_CTL (Fig. 4a, 4b). Despite the
446 suppression of these source terms, the substantial enhancement of snow deposition
447 growth dominates the snow budget in layer A, resulting in a net increase in snow
448 production and cloud-snow mass concentration.

449 Finally, the ratio of cloud ice to cloud snow changes from 1:1 to 1:3 in layer A,
450 more closely consistent with observation, which shows that cloud ice generally has
451 higher number concentrations but lower mass concentrations than cloud snow (Gao et
452 al., 2020; Yang et al., 2021; Feng et al., 2021; Fang et al., 2022). In the aircraft
453 observations reported, small ice particles ($>50\ \mu\text{m}$) reached concentrations of up to 300
454 L^{-1} , whereas large ice crystals ($>600\ \mu\text{m}$) were only about 3 L^{-1} (Wang et al., 2023).
455 Despite their much lower number concentrations, the larger particles contributed more
456 to the ice mass due to their substantially greater size. In the present simulation, the cloud
457 ice number concentrations in T_IN reach on the order of $10^1\ \text{L}^{-1}$ in the main mixed-
458 phase layer, which is substantially higher than in T_CTL and closer to the observed
459 magnitudes, although still lower than some aircraft measurements.

460 In layer B, the snow mass concentration shows relatively small changes, ranging
461 from approximately 90% to 100% of T_CTL. From the perspective of cloud
462 microphysics, the mechanisms are similar to those in layer A. Despite the reduction of
463 Pidep, the Psdep increases to 130%–200% of T_CTL. At the same time, the decrease
464 in cloud ice mass continues to suppress Psaut and Psaci, resulting in a total snow
465 production rate of about 95% of T_CTL.

466 In layer C, although the model diagnostics indicate an enhancement in cloud-snow
467 production processes (production rate for accretion of rain by snow (Psacr) and

468 production rate for accretion of rain by cloud ice (P_{iacr}) and a reduction in the
469 production rate for accretion of snow by rain (P_{racs}), newly formed cloud snow cannot
470 be maintained because the temperature is already above 0°C which makes it
471 instantaneously melt, rapidly converting to rain. As a result, there is no significant
472 change in snow mass concentration in this layer.

473 **Cloud water and rainwater**

474 Cloud water and rainwater are mainly distributed in layer C (temperature
475 approximately -2°C to 18°C). In this layer, both cloud-water and rainwater mixing
476 ratios in T_IN are about 90%-95% of those in T_CTL . This small reduction is primarily
477 attributed to a weakening of the production rate of cloud droplets via CCN (P_{cact}),
478 which decreases by about 5% at T_IN relative to T_CTL , indicating a suppressed
479 conversion of water vapour into liquid water. As a consequence of the reduced cloud-
480 water content, the production rate for accretion of rainwater by cloud water (P_{racw}) is
481 also weakened by 5%–10%. Meanwhile, the conversion of rainwater into ice-phase
482 hydrometeors (P_{sacr} , P_{gacr} , and P_{iacr}) is enhanced. However, under the
483 thermodynamic conditions of layer C, temperatures exceed the melting thresholds of
484 ice-phase hydrometeors, the newly formed snow and graupel rapidly melt and are easily
485 converted back into rainwater. Consequently, these ice-phase conversion processes
486 contribute only marginally to the net change in rainwater mixing ratio.

487 Fig. 5 shows that, over dust-precipitation stations in both the NDSA and the DPA,
488 the introduction of the online aerosol-IN nucleation scheme leads to temperature
489 increases below 4 km, with changes of about 0.16 to 0.52 K, while the water vapour
490 mixing ratio changes by -0.04 to 0.2 g kg^{-1} during this 18:00 UTC 11 April to 18:00
491 UTC 12 April. These changes lead to a decrease in relative humidity within the warm-
492 cloud layer. The relative humidity averaged over the dust precipitation stations
493 decreases by up to 3 percentage points during this period in the DPA. In the NDSA, it
494 locally reduces by 6–7 percentage points over a 4 km area at 06:00 UTC 12 April. The
495 reduced relative humidity suppresses droplet activation and condensational growth,
496 thereby inhibiting the development of warm clouds in T_IN compared to T_CTL .

497 Overall, dust suppresses cloud development, reducing the total ice-phase
498 hydrometeor content in layer A to 70 – 85% of T_CTL, the total ice-phase hydrometeor
499 content in layer B to 85 – 91% of T_CTL, and the liquid-phase hydrometeor content in
500 layer C to 90 – 95% of T_CTL. Our results indicate that dust aerosols tend to suppress
501 cloud development in springtime dust-related precipitation over East Asia, where
502 precipitation is predominantly stratiform. Similar suppression effects have also been
503 reported in previous observational studies (Zhu et al., 2023).

504 3.3 Precipitation

505 The online aerosol–IN nucleation scheme can modulate the spatial distribution of
506 precipitation. Figure 6a shows the observed event-accumulated precipitation of DPA
507 stations, and Figure 6b shows the simulated event-accumulated precipitation of T_CTL.
508 In T_CTL, 18 of 43 stations in DPA exhibit overestimated simulation precipitation
509 compared to observations (overestimated stations), primarily located in areas near dust
510 sources area such as Gansu, Ningxia, Shaanxi, and Inner Mongolia, as well as
511 northeastern provinces including Shandong, Liaoning, Jilin, and Heilongjiang (Fig. 6b).
512 At these overestimated stations, the observed mean accumulated precipitation is
513 11.49 mm, while the simulated mean accumulated precipitation is 25.55 mm (Fig. 7),
514 with an average sMAPE of 45 %. The other 25 stations show underestimated simulated
515 precipitation compared to observations (underestimated stations), mainly distributed
516 across Hebei, Beijing, Henan, and the Yangtze River Basin downwind area of the dust
517 events (Fig. 6b). At underestimated stations, the observed mean accumulated
518 precipitation is 31.58 mm (Fig. 7), while the simulated value is only 4.63 mm, with an
519 average sMAPE of -64 %.

520 In T_IN, the online aerosol–IN nucleation scheme does not alter the overall pattern
521 of overestimation of precipitation north of 35° N and underestimation of precipitation
522 south of 35° N in T_CTL (Fig. 6d). However, compared to T_CTL, notable
523 improvements are mainly observed between 34° and 40° N. This is driven by the
524 process discussed in Section 3.2, in which dust in layer C suppresses P_{act}, thereby
525 reducing the overestimation of precipitation near dust source areas. sMAPE is reduced

526 by about 1–10% in areas near the dust source, resulting in more accurate forecasts
527 compared to both T_CTL (Fig. 6e, 6f).

528 Rather than being removed by precipitation or evaporation, the suppressed cloud
529 hydrometeors are transported downstream in T_IN. We calculate horizontal
530 hydrometeor fluxes across 116°E, 33°–50°N and 33°N, 103°–116°E from 12:00 UTC
531 on 12 April to 18:00 UTC on 13 April (Fig. 7). Over the entire 0–12 km layer, the total
532 hydrometeor flux slightly increases to about 102% of that in T_CTL.

533 Within the temperature range from 0 to -40 °C, the total horizontal hydrometeor
534 flux decreases by about 11 %, primarily due to a substantial reduction in cloud ice flux,
535 accompanied by increases in snow and graupel fluxes. In Layer A, the total hydrometeor
536 flux is about $4.4 \times 10^{-5} \text{ kg s}^{-1}$, corresponding to about 75 % of T_CTL. Cloud ice flux
537 drops sharply to about 8 % of T_CTL, while snow and graupel fluxes increase markedly
538 to about 19.8 times and 7.8 times, respectively. In Layer B, the total hydrometeor flux
539 is about $2.6 \times 10^{-6} \text{ kg s}^{-1}$, corresponding to about 93 % of T_CTL, with cloud ice flux
540 reduced to about 28 % of T_CTL, and snow and graupel fluxes increased to about 2.3
541 times and about 1.8 times, respectively. At temperatures above 0 °C, the total horizontal
542 hydrometeor flux increases to about 106 % of T_CTL, with cloud water and rainwater
543 fluxes increasing to about 115 % and about 108 %, respectively.

544 These results indicate that although dust suppresses cold-cloud development in the
545 upper and mid-troposphere, it enhances the downstream transport of liquid-phase
546 hydrometeors near and below the melting layer, enhancing downstream precipitation.
547 Finally, for underestimation stations, the mean accumulated precipitation increases by
548 1.1 mm compared to T_CTL, and precipitation simulation improves by approximately
549 4 %, with little changes in MAE and RMSE (Fig. 8b). For overestimated stations, the
550 mean accumulated precipitation decreases by 4.5 mm compared to T_CTL, and
551 precipitation simulations improves by approximately 40%, with MAE reduced by 1.4
552 and RMSE reduced by 4.1 (Fig. 8a).

553 In summary, because the reduction in cloud water in the 0–4 km layer is relatively
554 small, the corresponding decrease in rainwater reaching the surface is also limited. As

555 a result, the online aerosol-IN nucleation scheme exerts only a weak influence on the
556 total precipitation amount. Nevertheless, it can modulate the spatial and temporal
557 distribution of precipitation, impressing overestimates and altering underestimates to
558 some degree, which is consistent with the findings of Park and Lim (2023) and Su and
559 Fung (2018b).

560 **4 Conclusions and discussion**

561 To explore the impact of spring dust aerosols on precipitation, this study develops
562 an online aerosol-IN nucleation scheme within the regional model GRAPES/CUACE.
563 The model performance has been evaluated by a typical dust-precipitation event from
564 00:00 UTC on 9 April to 00:00 UTC on 15 April 2018.

565 Dust provides ice nuclei via heterogeneous nucleation during dust precipitation
566 events. The online aerosol-IN nucleation scheme significantly modifies the
567 distributions of nucleated IN concentrations. The original WDM6 scheme exhibits a
568 systematic underestimation of ice-nuclei concentrations, with nucleated IN
569 concentrations reaching 10^2 L^{-1} between 4 and 7 km altitude during the dust-
570 precipitation event, and abnormally increasing with height due to its temperature-
571 dependent formulation, peaking near the -40° C layer. With the online aerosol-IN
572 nucleation scheme, IN concentrations can reach 10^4 L^{-1} , so for the cloud ice mass
573 production rate, concentrated peaking at about the layer between 4 and 7 km in height,
574 closer to the observations

575 Dust can inhibit the development of clouds. Above 7 km, dust suppresses the
576 growth rate of cloud ice (through both heterogeneous nucleation and deposition-
577 sublimation rate of cloud ice), and the total production rate of cloud ice drops to less
578 than 24% of that in T_CTL, promoting snow formation and ultimately reducing the
579 total ice-phase hydrometeor content to 70–85% of T_CTL. Meanwhile, the total snow
580 production rate in T_IN increases to approximately 88-200% of that in T_CTL,
581 reducing the total ice-phase hydrometeor content to 70 – 85% of T_CTL. Between 4
582 and 7 km height, dust enhances heterogeneous nucleation of cloud ice, but the new,
583 smaller particles suppress cloud ice and reduce the deposition rate, resulting in the total

584 ice-phase hydrometeor content decreasing to 85–91% of T_CTL. Below 4 km in height,
585 the relative humidity decreases by about 3 percentage points on average over the dust-
586 precipitation stations in T_IN. This decrease in relative humidity limits the conversion
587 of water vapour to cloud water and of cloud water to rain, reducing the liquid-phase
588 hydrometeor content to 90–95% of that in T_CTL.

589 The dust can also modulate the spatial distribution of precipitation, even though
590 the online aerosol-IN nucleation scheme cannot fully alter the overall pattern of
591 precipitation overestimation north of 35° N and underestimation south of 35° N, as seen
592 in T_CTL. The online aerosol-IN nucleation scheme mitigates the overestimation of
593 precipitation near dust source areas. For overestimated stations, the event-mean
594 accumulated precipitation decreases by about 4.5 mm relative to T_CTL, with the MAE
595 reducing by 1.4, and the RMSE reducing by 4.1. Meanwhile, the cloud hydrometeors
596 suppressed by dust IN are not removed from the atmosphere; instead, they remain in
597 the weather system and are transported downstream as the air mass moves, thereby
598 alleviating the underestimation of precipitation in downstream areas. In stations where
599 precipitation is previously underestimated, the mean accumulated precipitation
600 increases by about 1.1 mm relative to T_CTL.

601 This study shows improvements in dust, IN on cloud, and precipitation simulations
602 using a comprehensive online aerosol-IN-cloud interaction scheme. Considering both
603 CCN and IN effects, rather than CCN alone, improves precipitation simulations by up
604 to approximately 40 %. Aerosol-cloud interactions are an old, open question, but many
605 uncertainties remain due to the complex mechanisms of both CCN and IN. Furthermore,
606 the scarcity of real-time observations hinders the in-depth exploration of detailed
607 microphysical processes and their underlying mechanisms. More cases across different
608 seasons and dust levels are needed in the future, with more observations.

609 **Code/data availability**

610 All source code and data can be accessed by contacting the corresponding author,
611 Chunhong Zhou (zhouch@cma.gov.cn) and Xiaoye Zhang (xiaoye@cma.gov.cn).

612 **Author contributions**

613 JZ developed the online aerosol-IN nucleation scheme, conducted the data analysis, and
614 wrote the original draft of this paper. CHZ developed the aerosol-CCN-cloud
615 interaction scheme and the online aerosol-IN nucleation scheme, and reviewed and
616 edited the manuscript, providing critical insights. XYS reviewed the manuscript. SLG
617 reviewed the manuscript and provided general insight. HW reviewed the manuscript.
618 XYZ reviewed the manuscript and gave guidance on the data analysis. All authors have
619 given approval to the final version of the paper.

620 **Competing interests**

621 The authors declare no conflicts of interest.

622 **Financial support**

623 This study was jointly supported by the NSFC Project (42090030), the National Key
624 Project of the Ministry of Science and Technology of China (2022YFC3701205), Four-
625 Dimensional Variational Quantitative Inversion of Carbon Dioxide Sources and Sinks
626 in the Ecosystem of the Sichuan Basin (2024JDHJ0058), A Study on the Integrated
627 Simulation System for the Interaction Between Greenhouse Gases and Air Quality in
628 Sichuan Province and the Science and Technology Development Fund of CAMS
629 (2023KJ003).

630 **Acknowledgements**

631 All figures in this study were produced using the open-source software MeteoInfoLab
632 (<http://www.meteothink.org/index.html>). The meteorological initial and boundary
633 conditions for the modelling system were obtained from the China Meteorological Data
634 Sharing Service System
635 (<http://data.cma.cn/data/cdcindex/cid/98c64da7ee348b37html>). The meteorological
636 observations were obtained from the China Meteorological Data Sharing Service
637 System (<http://data.cma.cn/data/cdcindex/cid/f0fb4b55508804ca.html>). The PM₁₀ and
638 PM_{2.5} concentration data were obtained from the national environmental monitoring
639 network of the Ministry of Ecology and Environment of China (<http://www.cnemc.cn>).
640 The NCEP/NCAR Final Operational Global Analysis (FNL) data, with a temporal

641 resolution of 6 hours and a spatial resolution of 0.25°
642 (<https://rda.ucar.edu/datasets/ds083.3/>). We are grateful to the two anonymous
643 reviewers for their thoughtful, detailed, constructive comments, which helped to
644 improve the clarity of the paper.

645 **References**

- 646 Albrecht, B. A.: Aerosols, Cloud Microphysics, and Fractional Cloudiness, *Science*, 245, 1227–
647 1230, <https://doi.org/10.1126/science.245.4923.1227>, 1989.
- 648 Alfaro, S. and Gomes, L.: Modeling mineral aerosol production by wind erosion: Emission
649 intensities and aerosol size distributions in source areas, *Journal of Geophysical Research*, 106,
650 18075–18084, <https://doi.org/10.1029/2000JD900339>, 2001.
- 651 Andreae, M. O. and Crutzen, P. J.: Atmospheric Aerosols: Biogeochemical Sources and Role in
652 Atmospheric Chemistry, *Science*, 276, 1052–1058,
653 <https://doi.org/10.1126/science.276.5315.1052>, 1997.
- 654 Bi, K., McMeeking, G. R., Ding, D. P., Levin, E. J. T., DeMott, P. J., Zhao, D. L., Wang, F., Liu, Q.,
655 Tian, P., Ma, X. C., Chen, Y. B., Huang, M. Y., Zhang, H. L., Gordon, T. D., and Chen, P.:
656 Measurements of Ice Nucleating Particles in Beijing, China, *Journal of Geophysical Research:*
657 *Atmospheres*, 124, 8065–8075, <https://doi.org/10.1029/2019JD030609>, 2019.
- 658 Boose, Y., Welti, A., Atkinson, J., Ramelli, F., Danielczok, A., Bingemer, H. G., Plötze, M., Sierau,
659 B., Kanji, Z. A., and Lohmann, U.: Heterogeneous ice nucleation on dust particles sourced
660 from nine deserts worldwide – Part 1: Immersion freezing, *Atmospheric Chemistry and Physics*,
661 16, 15075–15095, <https://doi.org/10.5194/acp-16-15075-2016>, 2016.
- 662 Cantrell, W., Bunker, K., Niehaus, J., China, S., Woodward, X., Kostinski, A., and Mazzoleni, C.:
663 Ice nucleation in the contact mode: Temperature and size dependence for selected dusts, *AIP*
664 *Conference Proceedings*, 1527, 926, <https://doi.org/10.1063/1.4803423>, 2013.
- 665 Che, Y., Zhang, J., Zhao, C., Fang, W., Xue, W., Yang, W., Ji, D., Dang, J., Duan, J., Sun, J., Shen,
666 X., and Zhou, X.: A study on the characteristics of ice nucleating particles concentration and
667 aerosols and their relationship in spring in Beijing, *Atmospheric Research*, 247, 105196,
668 <https://doi.org/10.1016/j.atmosres.2020.105196>, 2021.
- 669 Chen, D., Xue, J., Yang, X., Zhang, H., Shen, X., Hu, J., Wang, Y., Ji, L., and Chen, J.: New
670 generation of multi-scale NWP system (GRAPES): General scientific design, *Chinese Science*
671 *Bulletin*, 53, 3433–3445, <https://doi.org/10.1007/s11434-008-0494-z>, 2008.
- 672 Chen, J., Wu, Z., Chen, J., Reicher, N., Fang, X., Rudich, Y., and Hu, M.: Size-resolved atmospheric
673 ice-nucleating particles during East Asian dust events, *Atmospheric Chemistry and Physics*, 21,
674 3491–3506, <https://doi.org/10.5194/acp-21-3491-2021>, 2021.
- 675 Chen, J., Wu, Z., Meng, X., Zhang, C., Chen, J., Qiu, Y., Chen, L., Fang, X., Wang, Y., Zhang, Y.,
676 Chen, S., Gao, J., Li, W., and Hu, M.: Observational evidence for the non-suppression effect
677 of atmospheric chemical modification on the ice nucleation activity of East Asian dust, *Sci*
678 *Total Environ*, 861, 160708, <https://doi.org/10.1016/j.scitotenv.2022.160708>, 2023.
- 679 Chen, Q., Yin, Y., Jiang, H., Chu, Z., Xue, L., Shi, R., Zhang, X., and Chen, J.: The Roles of Mineral
680 Dust as Cloud Condensation Nuclei and Ice Nuclei During the Evolution of a Hail Storm,
681 *Journal of Geophysical Research Atmospheres*, 124, <https://doi.org/10.1029/2019JD031403>,

682 2019.

683 DeMott, P. J., Prenni, A. J., Liu, X., Kreidenweis, S. M., Petters, M. D., Twohy, C. H., Richardson,
684 M. S., Eidhammer, T., and Rogers, D. C.: Predicting global atmospheric ice nuclei distributions
685 and their impacts on climate, *Proceedings of the National Academy of Sciences*, 107, 11217–
686 11222, <https://doi.org/10.1073/pnas.0910818107>, 2010.

687 DeMott, P. J., Prenni, A. J., McMeeking, G. R., Sullivan, R. C., Petters, M. D., Tobo, Y., Niemand,
688 M., Möhler, O., Snider, J. R., Wang, Z., and Kreidenweis, S. M.: Integrating laboratory and
689 field data to quantify the immersion freezing ice nucleation activity of mineral dust particles,
690 *Atmospheric Chemistry and Physics*, 15, 393–409, <https://doi.org/10.5194/acp-15-393-2015>,
691 2015.

692 Eastwood, M. L., Cremel, S., Gehrke, C., Girard, E., and Bertram, A. K.: Ice nucleation on mineral
693 dust particles: Onset conditions, nucleation rates and contact angles, *Journal of Geophysical
694 Research: Atmospheres*, 113, <https://doi.org/10.1029/2008JD010639>, 2008.

695 Fan, J., Leung, L. R., DeMott, P. J., Comstock, J. M., Singh, B., Rosenfeld, D., Tomlinson, J. M.,
696 White, A., Prather, K. A., Minnis, P., Ayers, J. K., and Min, Q.: Aerosol impacts on California
697 winter clouds and precipitation during CalWater 2011: local pollution versus long-range
698 transported dust, *Atmospheric Chemistry and Physics*, 14, 81–101,
699 <https://doi.org/10.5194/acp-14-81-2014>, 2014.

700 Fang, W., Lou, X., Zhang, X., and Fu, Y.: Numerical Simulations of Cloud Number Concentration
701 and Ice Nuclei Influence on Cloud Processes and Seeding Effects, *Atmosphere*, 13, 1792,
702 <https://doi.org/10.3390/atmos13111792>, 2022.

703 Feng, Q., Niu, S., Hou, T., Fan, X., Shen, D., and Yang, J.: Aircraft—Based Observation of the
704 Physical Characteristics of Snowfall Cloud in Shanxi Province, *Chinese Journal of
705 Atmospheric Sciences (in Chinese)*, 45(5), 1146–1160, <https://doi.org/10.3878/j.issn.1006-9895.2106.21004>, 2021.

707 Filonchyk, M., Yan, H., Shareef, T. M. E., and Yang, S.: Aerosol contamination survey during dust
708 storm process in Northwestern China using ground, satellite observations and atmospheric
709 modeling data, *Theor Appl Climatol*, 135, 119–133, <https://doi.org/10.1007/s00704-017-2362-8>,
710 2019.

711 Gao, Q., Guo, X., He, H., Liu, X., Huang, M., and Ma, X.: Numerical Simulation Study on the
712 Microphysical Characteristics of Stratiform Clouds with Embedded Convections in Northern
713 China based on Aircraft Measurements, *Chinese Journal of Atmospheric Sciences(in Chinese)*,
714 44, 899–912, <https://doi.org/10.3878/j.issn.1006-9895.1908.19114>, 2020.

715 Gibbons, M., Min, Q., and Fan, J.: Investigating the impacts of Saharan dust on tropical deep
716 convection using spectral bin microphysics, *Atmospheric Chemistry and Physics*, 18, 12161–
717 12184, <https://doi.org/10.5194/acp-18-12161-2018>, 2018.

718 Gong, S. L. and Zhang, X. Y.: CUACE/Dust - an integrated system of observation and modeling
719 systems for operational dust forecasting in Asia, *Atmospheric Chemistry and Physics*, 8, 2333–
720 2340, 2008.

721 Gong, S. L., Zhang, X. Y., Zhao, T. L., McKendry, I. G., Jaffe, D. A., and Lu, N. M.: Characterization
722 of soil dust aerosol in China and its transport and distribution during 2001 ACE-Asia: 2. Model
723 simulation and validation, *Journal of Geophysical Research: Atmospheres*, 108,
724 <https://doi.org/10.1029/2002JD002633>, 2003.

725 Haarig, M., Ansmann, A., Walser, A., Baars, H., Urbanneck, C., Weinzierl, B., Schöberl, M., Dollner,

726 M., Mamouri, R., and Althausen, D.: Estimation of dust related ice nucleating particles in the
727 atmosphere: Comparison of profiling and in-situ measurements, *E3S Web Conf.*, 99, 04002,
728 <https://doi.org/10.1051/e3sconf/20199904002>, 2019.

729 He, C., Yin, Y., Huang, Y., Kuang, X., Cui, Y., Chen, K., Jiang, H., Kiselev, A., Möhler, O., and
730 Schrod, J.: The Vertical Distribution of Ice-Nucleating Particles over the North China Plain: A
731 Case of Cold Front Passage, *Remote Sensing*, 15, 4989, <https://doi.org/10.3390/rs15204989>,
732 2023.

733 He, Y., Zhang, Y., Liu, F., Yin, Z., Yi, Y., Zhan, Y., and Yi, F.: Retrievals of dust-related particle mass
734 and ice-nucleating particle concentration profiles with ground-based polarization lidar and sun
735 photometer over a megacity in central China, *Atmospheric Measurement Techniques*, 14,
736 5939–5954, <https://doi.org/10.5194/amt-14-5939-2021>, 2021.

737 Herbert, R. J., Murray, B. J., Dobbie, S. J., and Koop, T.: Sensitivity of liquid clouds to homogenous
738 freezing parameterizations, *Geophys. Res. Lett.*, 42, 1599–1605,
739 <https://doi.org/10.1002/2014GL062729>, 2015.

740 Hiranuma, N., Augustin-Bauditz, S., Bingemer, H., Budke, C., Curtius, J., Danielczok, A., Diehl,
741 K., Dreischmeier, K., Ebert, M., Frank, F., Hoffmann, N., Kandler, K., Kiselev, A., Koop, T.,
742 Leisner, T., Möhler, O., Nillius, B., Peckhaus, A., Rose, D., Weinbruch, S., Wex, H., Boose, Y.,
743 DeMott, P. J., Hader, J. D., Hill, T. C. J., Kanji, Z. A., Kulkarni, G., Levin, E. J. T., McCluskey,
744 C. S., Murakami, M., Murray, B. J., Niedermeier, D., Petters, M. D., O’Sullivan, D., Saito, A.,
745 Schill, G. P., Tajiri, T., Tolbert, M. A., Welti, A., Whale, T. F., Wright, T. P., and Yamashita, K.:
746 A comprehensive laboratory study on the immersion freezing behavior of illite NX particles: a
747 comparison of 17 ice nucleation measurement techniques, *Atmospheric Chemistry and Physics*,
748 15, 2489–2518, <https://doi.org/10.5194/acp-15-2489-2015>, 2015.

749 Hong, S.-Y., Dudhia, J., and Chen, S.-H.: A Revised Approach to Ice Microphysical Processes for
750 the Bulk Parameterization of Clouds and Precipitation, *Monthly Weather Review*, 132, 103–
751 120, [https://doi.org/10.1175/1520-0493\(2004\)132<0103:ARATIM>2.0.CO;2](https://doi.org/10.1175/1520-0493(2004)132<0103:ARATIM>2.0.CO;2), 2004.

752 Hu, Y., Tian, P., Huang, M., Bi, K., Schneider, J., Umo, N. S., Ullmerich, N., Höhler, K., Jing, X.,
753 Xue, H., Ding, D., Liu, Y., Leisner, T., and Möhler, O.: Characteristics of ice-nucleating
754 particles in Beijing during spring: A comparison study of measurements between the suburban
755 and a nearby mountain area, *Atmospheric Environment*, 293, 119451,
756 <https://doi.org/10.1016/j.atmosenv.2022.119451>, 2023.

757 Igel, A. L., Igel, M. R., and Heever, S. C. van den: Make It a Double? Sobering Results from
758 Simulations Using Single-Moment Microphysics Schemes, *Journal of the Atmospheric
759 Sciences*, 72, 910–925, <https://doi.org/10.1175/JAS-D-14-0107.1>, 2015.

760 Ilotoviz, E., Khain, A. P., Benmoshe, N., Phillips, V. T. J., and Ryzhkov, A. V.: Effect of Aerosols on
761 Freezing Drops, Hail, and Precipitation in a Midlatitude Storm, *Journal of the Atmospheric
762 Sciences*, 73, 109–144, <https://doi.org/10.1175/JAS-D-14-0155.1>, 2016.

763 Jiang, H., Yin, Y., Su, H., Shan, Y., and Gao, R.: The characteristics of atmospheric ice nuclei
764 measured at the top of Huangshan (the Yellow Mountains) in Southeast China using a newly
765 built static vacuum water vapor diffusion chamber, *Atmospheric Research*, 153, 200–208,
766 <https://doi.org/10.1016/j.atmosres.2014.08.015>, 2015.

767 Jiang, H., Yin, Y., Wang, X., Gao, R., Yuan, L., Chen, K., and Shan, Y.: The measurement and
768 parameterization of ice nucleating particles in different backgrounds of China, *Atmospheric
769 Research*, 181, 72–80, <https://doi.org/10.1016/j.atmosres.2016.06.013>, 2016.

770 Kang, J.-Y., Yoon, S., Shao, Y., and Kim, S.-W.: Comparison of vertical dust flux by implementing
771 three dust emission schemes in WRF/Chem, *Journal of Geophysical Research*, 116,
772 <https://doi.org/10.1029/2010JD014649>, 2011.

773 Kang, Y., Jin, S., Peng, X., Yang, X., Shang, K., and Wang, S.: Comparative Analysis of Single-
774 Moment and Double-Moment Microphysics Schemes in WRF on the Torrential Rainfall Event
775 in North China During 1921 July, 2016, *Plateau Meteorology*, 37, 481–494, 2018.

776 Kanji, Z. A., Ladino, L. A., Wex, H., Boose, Y., Burkert-Kohn, M., Cziczo, D. J., and Krämer, M.:
777 Overview of Ice Nucleating Particles, [https://doi.org/10.1175/AMSMONOGRAPHS-D-16-](https://doi.org/10.1175/AMSMONOGRAPHS-D-16-0006.1)
778 [0006.1](https://doi.org/10.1175/AMSMONOGRAPHS-D-16-0006.1), 2017.

779 Kaufman, Y. J., Tanré, D., and Boucher, O.: A satellite view of aerosols in the climate system, *Nature*,
780 419, 215–223, <https://doi.org/10.1038/nature01091>, 2002.

781 Khain, A., Ovtchinnikov, M., Pinsky, M., Pokrovsky, A., and Krugliak, H.: Notes on the state-of-
782 the-art numerical modeling of cloud microphysics, *Atmospheric Research*, 55, 159–224,
783 [https://doi.org/10.1016/S0169-8095\(00\)00064-8](https://doi.org/10.1016/S0169-8095(00)00064-8), 2000.

784 Knopf, D. A. and Alpert, P. A.: Atmospheric ice nucleation, *Nat Rev Phys*, 5, 203–217,
785 <https://doi.org/10.1038/s42254-023-00570-7>, 2023.

786 Kumar, V. A., Pandithurai, G., Kulkarni, G., Hazra, A., Patil, S. S., Dudhambe, S. D., Patil, R. D.,
787 Chen, J.-P., and Niranjana, K.: Atmospheric ice nuclei concentration measurements over a high
788 altitude-station in the Western Ghats, India, *Atmospheric Research*, 235, 104795,
789 <https://doi.org/10.1016/j.atmosres.2019.104795>, 2020.

790 Lee, S. S., Kim, B.-G., Yum, S. S., Seo, K.-H., Jung, C.-H., Um, J. S., Li, Z., Hong, J., Chang, K.-
791 H., and Jeong, J.-Y.: Effects of aerosol on evaporation, freezing and precipitation in a multiple
792 cloud system, *Clim Dyn*, 48, 1069–1087, <https://doi.org/10.1007/s00382-016-3128-1>, 2017.

793 Li, J., Liu, W., Castarède, D., Gu, W., Li, L., Ohigashi, T., Zhang, G., Tang, M., Thomson, E. S.,
794 Hallquist, M., Wang, S., and Kong, X.: Hygroscopicity and Ice Nucleation Properties of
795 Dust/Salt Mixtures Originating from the Source of East Asian Dust Storms, *Front. Environ.*
796 *Sci.*, 10, <https://doi.org/10.3389/fenvs.2022.897127>, 2022.

797 Li, M., Zhang, Q., Kurokawa, J., Woo, J.-H., He, K., Lu, Z., Ohara, T., Song, Y., Streets, D. G.,
798 Carmichael, G. R., Cheng, Y., Hong, C., Huo, H., Jiang, X., Kang, S., Liu, F., Su, H., and Zheng,
799 B.: MIX: a mosaic Asian anthropogenic emission inventory under the international
800 collaboration framework of the MICS-Asia and HTAP, *Atmospheric Chemistry and Physics*,
801 17, 935–963, <https://doi.org/10.5194/acp-17-935-2017>, 2017.

802 Liu, H., Yu, Y., Xia, D., Zhao, S., Ma, X., and Dong, L.: Analysis of the relationship between dust
803 aerosol and precipitation in spring over East Asia using EOF and SVD methods, *Science of*
804 *The Total Environment*, 908, 168437, <https://doi.org/10.1016/j.scitotenv.2023.168437>, 2024.

805 Marticorena, B. and Bergametti, G.: Modeling the atmospheric dust cycle: 1. Design of a soil-
806 derived dust emission scheme, *Journal of Geophysical Research: Atmospheres*, 100, 16415–
807 16430, <https://doi.org/10.1029/95JD00690>, 1995.

808 Mascioli, N. R., Evan, A. T., and Ralph, F. M.: Influence of Dust on Precipitation During Landfalling
809 Atmospheric Rivers in an Idealized Framework, *Journal of Geophysical Research:*
810 *Atmospheres*, 126, e2021JD034813, <https://doi.org/10.1029/2021JD034813>, 2021.

811 Molthan, A. L. and Colle, B. A.: Comparisons of Single- and Double-Moment Microphysics
812 Schemes in the Simulation of a Synoptic-Scale Snowfall Event, *Monthly Weather Review*, 140,
813 2982–3002, <https://doi.org/10.1175/MWR-D-11-00292.1>, 2012.

814 Naeger, A. R.: Impact of dust aerosols on precipitation associated with atmospheric rivers using
815 WRF-Chem simulations, *Results in Physics*, 10, 217–221,
816 <https://doi.org/10.1016/j.rinp.2018.05.027>, 2018.

817 Nenes, A., Murray, B., and Bougiatioti, A.: Mineral Dust and its Microphysical Interactions with
818 Clouds, *Mineral Dust: A Key Player in the Earth System*, 287–325,
819 https://doi.org/10.1007/978-94-017-8978-3_12, 2014.

820 Niehaus, J., Becker, J. G., Kostinski, A., and Cantrell, W.: Laboratory Measurements of Contact
821 Freezing by Dust and Bacteria at Temperatures of Mixed-Phase Clouds, *Journal of the*
822 *Atmospheric Sciences*, 71, 3659–3667, <https://doi.org/10.1175/JAS-D-14-0022.1>, 2014.

823 Pan, X., Uno, I., Wang, Z., Nishizawa, T., Sugimoto, N., Yamamoto, S., Kobayashi, H., Sun, Y., Fu,
824 P., Tang, X., and Wang, Z.: Real-time observational evidence of changing Asian dust
825 morphology with the mixing of heavy anthropogenic pollution, *Sci Rep*, 7, 335,
826 <https://doi.org/10.1038/s41598-017-00444-w>, 2017.

827 Park, S.-Y. and Lim, K.-S. S.: Implementation of Prognostic Cloud Ice Number Concentrations for
828 the Weather Research and Forecasting (WRF) Double-Moment 6-Class (WDM6)
829 Microphysics Scheme, *Journal of Advances in Modeling Earth Systems*, 15, e2022MS003009,
830 <https://doi.org/10.1029/2022MS003009>, 2023.

831 Patnaude, R. J., McCluskey, C. S., Roberts, G. C., DeMott, P. J., Hill, T. C. J., McFarquhar, G. M.,
832 Kollias, P., Ranjbar, K., Wolde, M., and Kreidenweis, S. M.: Characteristics of Ice Nucleating
833 Particles From the Long-Range Transport of Saharan Dust, *Geophysical Research Letters*, 52,
834 e2024GL113365, <https://doi.org/10.1029/2024GL113365>, 2025.

835 Possner, A., Ekman, A. M. L., and Lohmann, U.: Cloud response and feedback processes in
836 stratiform mixed-phase clouds perturbed by ship exhaust, *Geophysical Research Letters*, 44,
837 1964–1972, <https://doi.org/10.1002/2016GL071358>, 2017.

838 Pu, Z. and Lin, C.: Evaluation of double-moment representation of ice hydrometeors in bulk
839 microphysical parameterization: comparison between WRF numerical simulations and UND-
840 Citation data during MC3E, *Geosci. Lett.*, 2, 11, <https://doi.org/10.1186/s40562-015-0028-x>,
841 2015.

842 Shao, Y., Ishizuka, M., Mikami, M., and Leys, J. F.: Parameterization of size-resolved dust emission
843 and validation with measurements, *Journal of Geophysical Research: Atmospheres*, 116,
844 <https://doi.org/10.1029/2010JD014527>, 2011.

845 Shcherbakov, M., Brebels, A., Shcherbakova, N. L., Tyukov, A., Janovsky, T. A., and Kamaev, V.
846 A.: A survey of forecast error measures, *World Applied Sciences Journal*, 24, 171–176,
847 <https://doi.org/10.5829/idosi.wasj.2013.24.itmies.80032>, 2013.

848 Shen, X., Shi, Y., Wang, H., Zhang, M., and Han, J.: Comparison of two double-moment cloud
849 microphysics schemes in the GRAPES_Meso model on simulating a cold cloud process,
850 *Torrential Rain and Disasters*, 41, 336–347, <https://doi.org/10.3969/j.issn.1004-9045.2022.03.010>, 2022.

852 Shen, X., Mei, H., Wang, W., and Huang, W.: Numerical Simulation of Ice-Phase Processes Using
853 a Double-Moment Microphysical Scheme and a Sensitivity Test of Ice Nuclei Concentration,
854 *Chinese Journal of Atmospheric Sciences*, 39, 83–99, <https://doi.org/10.3878/j.issn.1006-9895.1405.13310>, 2024.

856 Stevens, R. G., Loewe, K., Dearden, C., Dimitrellos, A., Possner, A., Eirund, G. K., Raatikainen, T.,
857 Hill, A. A., Shipway, B. J., Wilkinson, J., Romakkaniemi, S., Tonttila, J., Laaksonen, A.,

858 Korhonen, H., Connolly, P., Lohmann, U., Hoose, C., Ekman, A. M. L., Carslaw, K. S., and
859 Field, P. R.: A model intercomparison of CCN-limited tenuous clouds in the high Arctic,
860 *Atmospheric Chemistry and Physics*, 18, 11041–11071, [https://doi.org/10.5194/acp-18-11041-](https://doi.org/10.5194/acp-18-11041-2018)
861 2018, 2018.

862 Stier, P., van den Heever, S. C., Christensen, M. W., Gryspeerdt, E., Dagan, G., Saleeby, S. M.,
863 Bollasina, M., Donner, L., Emanuel, K., Ekman, A. M. L., Feingold, G., Field, P., Forster, P.,
864 Haywood, J., Kahn, R., Koren, I., Kummerow, C., L'Ecuyer, T., Lohmann, U., Ming, Y., Myhre,
865 G., Quaas, J., Rosenfeld, D., Samset, B., Seifert, A., Stephens, G., and Tao, W.-K.: Multifaceted
866 aerosol effects on precipitation, *Nat. Geosci.*, 17, 719–732, [https://doi.org/10.1038/s41561-](https://doi.org/10.1038/s41561-024-01482-6)
867 024-01482-6, 2024.

868 Stith, J. L., Ramanathan, V., Cooper, W. A., Roberts, G. C., DeMott, P. J., Carmichael, G., Hatch, C.
869 D., Adhikary, B., Twohy, C. H., Rogers, D. C., Baumgardner, D., Prenni, A. J., Campos, T.,
870 Gao, R., Anderson, J., and Feng, Y.: An overview of aircraft observations from the Pacific Dust
871 Experiment campaign, *Journal of Geophysical Research: Atmospheres*, 114,
872 <https://doi.org/10.1029/2008JD010924>, 2009.

873 Su, L. and Fung, J. C. H.: Investigating the role of dust in ice nucleation within clouds and further
874 effects on the regional weather system over East Asia – Part 1: model development and
875 validation, *Atmospheric Chemistry and Physics*, 18, 8707–8725, [https://doi.org/10.5194/acp-](https://doi.org/10.5194/acp-18-8707-2018)
876 18-8707-2018, 2018a.

877 Su, L. and Fung, J. C. H.: Investigating the role of dust in ice nucleation within clouds and further
878 effects on the regional weather system over East Asia – Part 2: modification of the weather
879 system, *Atmospheric Chemistry and Physics*, 18, 11529–11545, [https://doi.org/10.5194/acp-](https://doi.org/10.5194/acp-18-11529-2018)
880 18-11529-2018, 2018b.

881 Tobo, Y., Adachi, K., DeMott, P. J., Hill, T. C. J., Hamilton, D. S., Mahowald, N. M., Nagatsuka, N.,
882 Ohata, S., Uetake, J., Kondo, Y., and Koike, M.: Glacially sourced dust as a potentially
883 significant source of ice nucleating particles, *Nat. Geosci.*, 12, 253–258,
884 <https://doi.org/10.1038/s41561-019-0314-x>, 2019.

885 Tobo, Y., Uetake, J., Matsui, H., Moteki, N., Uji, Y., Iwamoto, Y., Miura, K., and Misumi, R.:
886 Seasonal Trends of Atmospheric Ice Nucleating Particles Over Tokyo, *Journal of Geophysical*
887 *Research: Atmospheres*, 125, e2020JD033658, <https://doi.org/10.1029/2020JD033658>, 2020.

888 Trochkin, D., Iwasaka, Y., Matsuki, A., Yamada, M., Kim, Y.-S., Nagatani, T., Zhang, D., Shi, G.-
889 Y., and Shen, Z.: Mineral aerosol particles collected in Dunhuang, China, and their comparison
890 with chemically modified particles collected over Japan, *Journal of Geophysical Research:*
891 *Atmospheres*, 108, <https://doi.org/10.1029/2002JD003268>, 2003.

892 Um, J., McFarquhar, G. M., Stith, J. L., Jung, C. H., Lee, S. S., Lee, J. Y., Shin, Y., Lee, Y. G., Yang,
893 Y. I., Yum, S. S., Kim, B.-G., Cha, J. W., and Ko, A.-R.: Microphysical characteristics of frozen
894 droplet aggregates from deep convective clouds, *Atmospheric Chemistry and Physics*, 18,
895 16915–16930, <https://doi.org/10.5194/acp-18-16915-2018>, 2018.

896 Wang, H., Gong, S. L., Zhang, H. L., Chen, Y., Shen, X. S., Chen, D. H., Xue, J. S., Shen, Y. F., and
897 Jin, W. Z.: A new-generation sand and dust storm forecasting system GRAPES_CUACE/Dust:
898 Model development, verification and numerical simulation, *Chinese Science Bulletin*,
899 <https://doi.org/10.1007/s11434-009-0481-z>, 2010.

900 Wang, H., Zhang, X. Y., Wang, P., Peng, Y., Zhang, W. J., Liu, Z. D., Han, C., Li, S. T., Wang, Y. Q.,
901 Che, H. Z., Huang, L. P., Liu, H. L., Zhang, L., Zhou, C. H., Ma, Z. S., Chen, F. F., Ma, X.,

902 Wu, X. J., Zhang, B. H., and Shen, X. S.: Chemistry-Weather Interacted Model System
903 GRAPES_Meso5.1/CUACE CW V1.0: Development, Evaluation and Application in Better
904 Haze/Fog Prediction in China, *Journal of Advances in Modeling Earth Systems*, 14,
905 e2022MS003222, <https://doi.org/10.1029/2022MS003222>, 2022.

906 Wang, J., Wang, T., Yasheng, D., Wang, X., Lei, Y., Li, X., Wang, Z., and Shi, B.: Modulations of
907 dust aerosols on precipitation: Evidence from a typical heavy sandstorm event, *Atmospheric
908 Research*, 304, 107411, <https://doi.org/10.1016/j.atmosres.2024.107411>, 2024.

909 Wang, W., Sheng, L., Jin, H., and Han, Y.: Dust aerosol effects on cirrus and altocumulus clouds in
910 Northwest China, *J Meteorol Res*, 29, 793–805, <https://doi.org/10.1007/s13351-015-4116-9>,
911 2015.

912 Wang, Y. and Yan, Z.: Effect of Different Verification Schemes on Precipitation Verification and
913 Assessment Conclusion, *Meteorological Monthly*, 33, 9, 53-61,
914 <https://doi.org/10.3969/j.issn.1000-0526.2007.12.008>, 2007.

915 Wang, Y., Kong, R., Cai, M., Zhou, Y., Song, C., Liu, S., Li, Q., Chen, H., and Zhao, C.: High small
916 ice concentration in stratiform clouds over Eastern China based on aircraft observations: Habit
917 properties and potential roles of secondary ice production, *Atmospheric Research*, 281, 106495,
918 <https://doi.org/10.1016/j.atmosres.2022.106495>, 2023.

919 Xu, G. Q., Chen, D. H., Xue, J. S., Sun, J., and Wang, S. Y.: The program structure designing and
920 optimizing tests of GRAPES physics, *Chinese Science Bulletin*, 53, 7,
921 <https://doi.org/10.1007/s11434-008-0418-y>, 2008.

922 Yang, J., Hu, X., Lei, H., Duan, Y., Lv, F., and Zhao, L.: Airborne Observations of Microphysical
923 Characteristics of Stratiform Cloud Over Eastern Side of Taihang Mountains, *Chinese Journal
924 of Atmospheric Sciences*, 45(1), 88–106, 2021.

925 Yang, L., Yin, Y., Yang, S., Jiang, H., Xiao, H., Chen, Q., Su, H., and Chen, C.: Measurement and
926 Analysis of Atmospheric Ice Nuclei in Nanjing, *CJAS*, 37, 579–594,
927 <https://doi.org/10.3878/j.issn.1006-9895.2012.11242>, 2013.

928 Zhang, M., Yu, H., Guo, J., Shen, X., Su, Y., Xue, H., and Dou, B.: Assessment on Unsystematic
929 Errors of GRAPES_GFS 2.0, *Journal of Applied Meteorological Science*, 30, 332–344, 2019.

930 Zhang, W., Wang, H., Zhang, X., Huang, L., Peng, Y., Liu, Z., Zhang, X., and Che, H.: Aerosol–
931 cloud interaction in the atmospheric chemistry model GRAPES_Meso5.1/CUACE and its
932 impacts on mesoscale numerical weather prediction under haze pollution conditions in Jing–
933 Jin–Ji in China, *Atmospheric Chemistry and Physics*, 22, 15207–15221,
934 <https://doi.org/10.5194/acp-22-15207-2022>, 2022.

935 Zhang, Z. and Shen, X.: On the development of the GRAPES——A new generation of the national
936 operational NWP system in China, *Chinese Science Bulletin*, 53, 4,
937 <https://doi.org/10.1007/s11434-008-0462-7>, 2008.

938 Zhao, X., Lin, Y., Luo, Y., Qian, Q., Liu, X., Liu, X., and Colle, B. A.: A Double-Moment SBU-
939 YLIN Cloud Microphysics Scheme and Its Impact on a Squall Line Simulation, *Journal of
940 Advances in Modeling Earth Systems*, 13, e2021MS002545,
941 <https://doi.org/10.1029/2021MS002545>, 2021.

942 Zhou, C., Zhang, X., Gong, S., Wang, Y., and Xue, M.: Improving aerosol interaction with clouds
943 and precipitation in a regional chemical weather modeling system, *Atmospheric Chemistry and
944 Physics*, 16, 145–160, <https://doi.org/10.5194/acp-16-145-2016>, 2016.

945 Zhou, C., Gui, H., Hu, J., Ke, H., Wang, Y., and Zhang, X.: Detection of New Dust Sources in

946 Central/East Asia and Their Impact on Simulations of a Severe Sand and Dust Storm, *Journal*
947 *of Geophysical Research: Atmospheres*, 124, 10232–10247,
948 <https://doi.org/10.1029/2019JD030753>, 2019.

949 Zhou, C., Rao, X., Sheng, L., Zhang, J., Lu, Lin, J., Hu, J., Zhang, B., and Xu, R.: Application of
950 Scale-adaptive Dust Emission Scheme to CMA-CUACE/Dust, *J Appl Meteor Sci*, 35, 400–
951 413, <https://doi.org/10.11898/1001-7313.20240402>, 2024.

952 Zhou, C., Gong, S., Zhang, X., Wang, Y., Niu, T., Liu, H., Zhao, T., Yang, Y., and Hou, Q.:
953 Development and evaluation of an operational SDS forecasting system for East Asia:
954 CUACE/Dust, *Atmospheric Chemistry and Physics*, 8, 787–798, [https://doi.org/10.5194/acp-](https://doi.org/10.5194/acp-8-787-2008)
955 [8-787-2008](https://doi.org/10.5194/acp-8-787-2008), 2008.

956 Zhou, C., Gong, S., Zhang, X., Liu, H., Xue, M., Cao, G., An, X., Che, H., Zhang, Y., and Niu, T.:
957 Towards the improvements of simulating the chemical and optical properties of Chinese
958 aerosols using an online coupled model – CUACE/Aero, *Tellus B: Chemical and Physical*
959 *Meteorology*, 64, 18965, <https://doi.org/10.3402/tellusb.v64i0.18965>, 2012.

960 Zhu, H., Li, R., Yang, S., Zhao, C., Jiang, Z., and Huang, C.: The impacts of dust aerosol and
961 convective available potential energy on precipitation vertical structure in southeastern China
962 as seen from multisource observations, *Atmospheric Chemistry and Physics*, 23, 2421–2437,
963 <https://doi.org/10.5194/acp-23-2421-2023>, 2023.

964
965

966 **Figure**

967 Figure 1

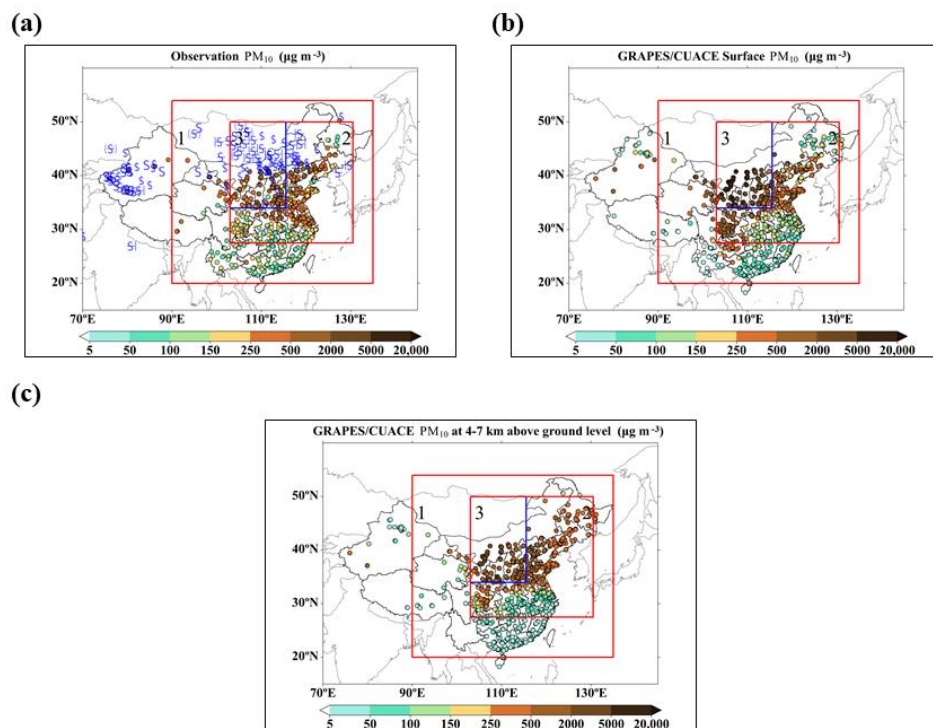


Figure 1. Observed and simulated affected areas of the dust events from 11 to 15 April. (region 1 is DA; region 2 is DPA; region 3 is NDSA)

(a) Observed distribution of most sever dusty weather phenomena and maximum PM₁₀ concentration for each station during the test time;

(b) Same as (a) but for maximum PM₁₀ concentration by GRAPES/CUACE;

(c) Maximum PM₁₀ concentration distribution in the layer of 4-7 km in height by GRAPES/CUACE

968

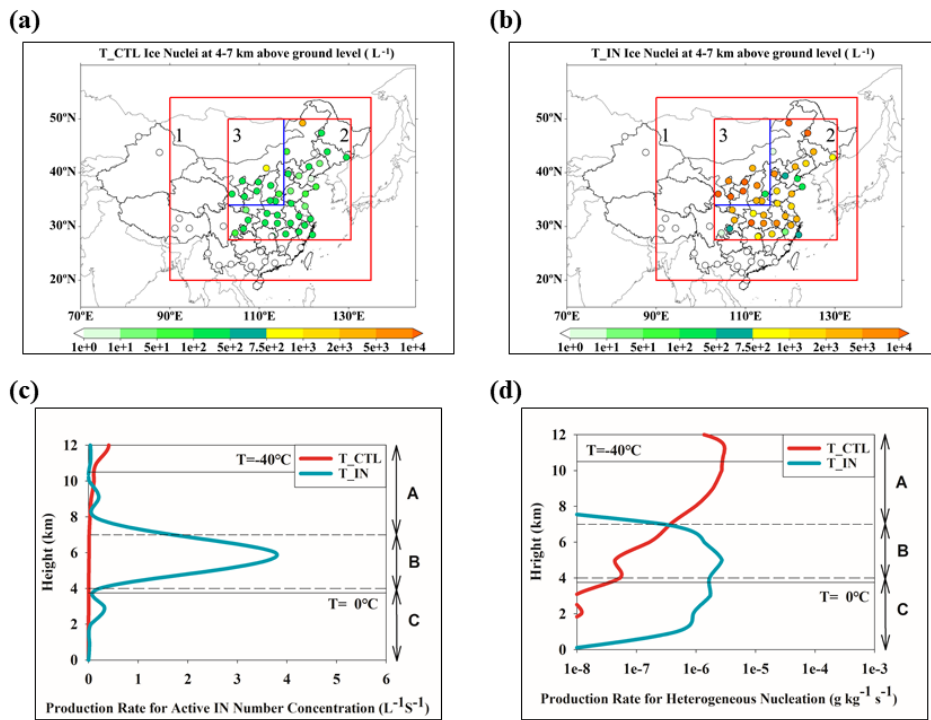


Figure 2. Distribution of IN from 11 to 15 April. (a) Maximum nucleated IN number concentration at 3-5 km altitude in T_CTL at DP stations; (b) Same as (a) but for T_IN simulations; (c) DP-event-averaged production rate for nucleated IN number concentration for T_CTL (red line) and T_IN (blue line); (d) DP-event-averaged vertical distribution of cloud ice mass production rate for heterogeneous ice nucleation for T_CTL (red line) and T_IN (blue line).

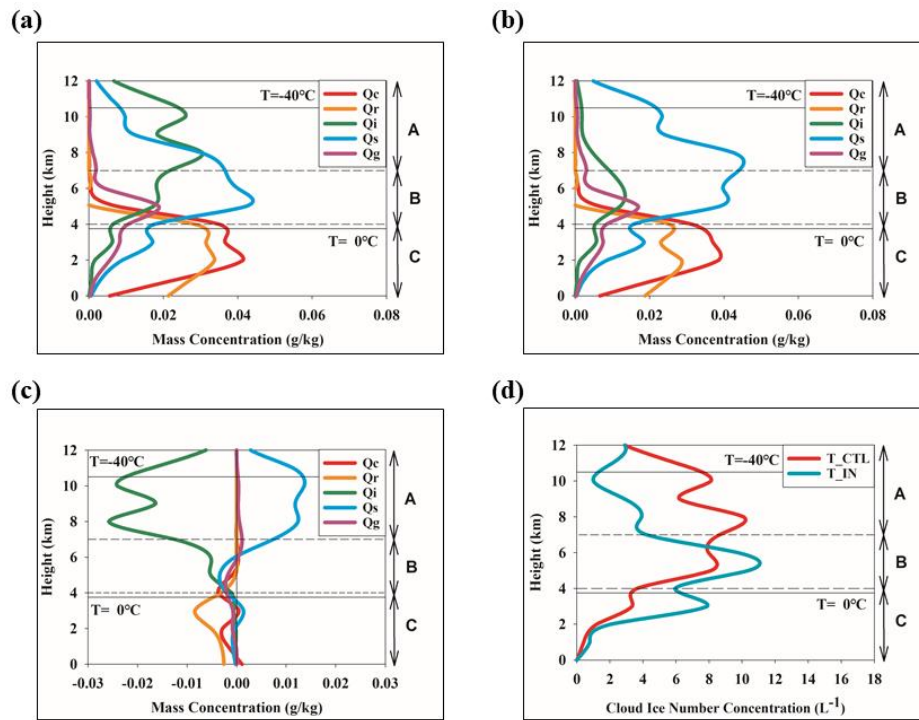


Figure 3. Distributions of hydrometeors, averaged over the dust–precipitation period (00 UTC 11 April–00 UTC 15 April 2018) and over dust–precipitation stations:

(a) hydrometeors simulated in T_CTL (b) hydrometeors simulated in T_IN

(c) hydrometeors difference by (T_IN- T_CTL);

(d) DP event-averaged vertical distributions of cloud ice number concentration

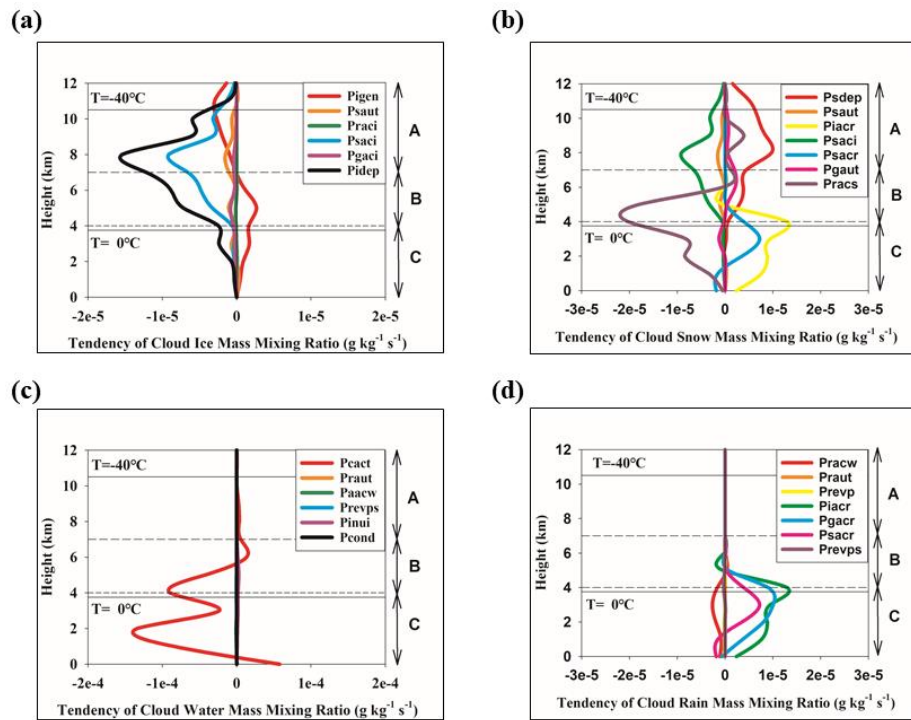


Figure 4. Vertical distributions of production rate difference for hydrometeors, averaged over the dust–precipitation period (00 UTC 11 April–00 UTC 15 April 2018) and over dust–precipitation stations:

- (a) production rate difference for cloud ice
- (b) production rate difference for cloud snow
- (c) production rate difference for cloud water
- (d) production rate difference for cloud rain

974

975

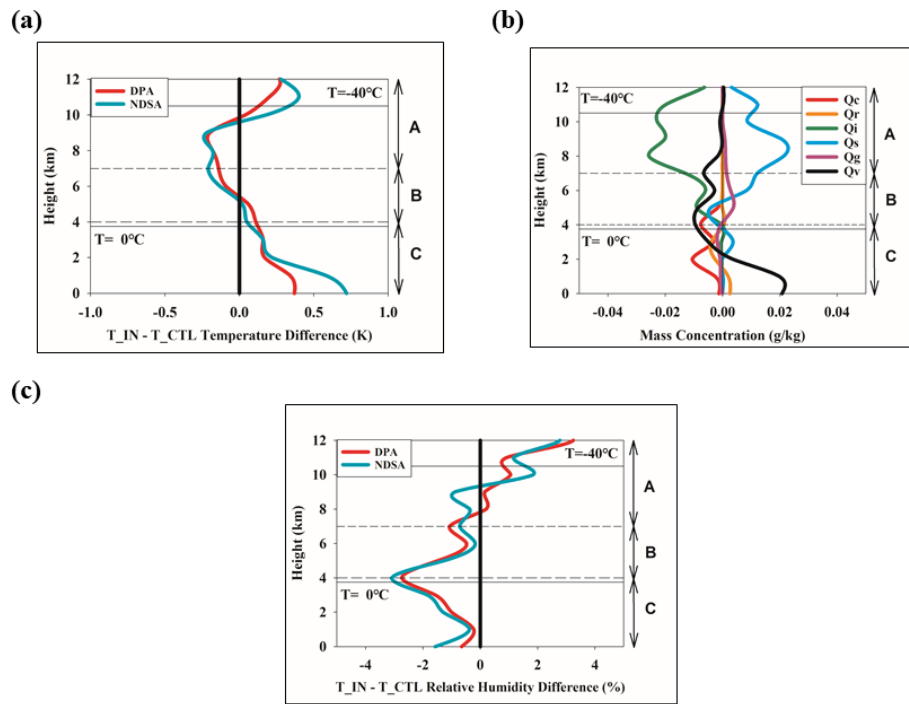


Figure 5. Vertical distributions of temperature difference and relative humidity difference, averaged over dust-precipitation stations from 18:00 UTC 11 April to 18:00 UTC 12 April:

(a) Temperature difference ($T_{IN} - T_{CTL}$)

(b) Differences in hydrometeor and water vapor mixing ratios ($T_{IN} - T_{CTL}$). For clarity, the water vapor changes are scaled to one-tenth of their actual values.

(c) Relative humidity difference ($T_{IN} - T_{CTL}$)

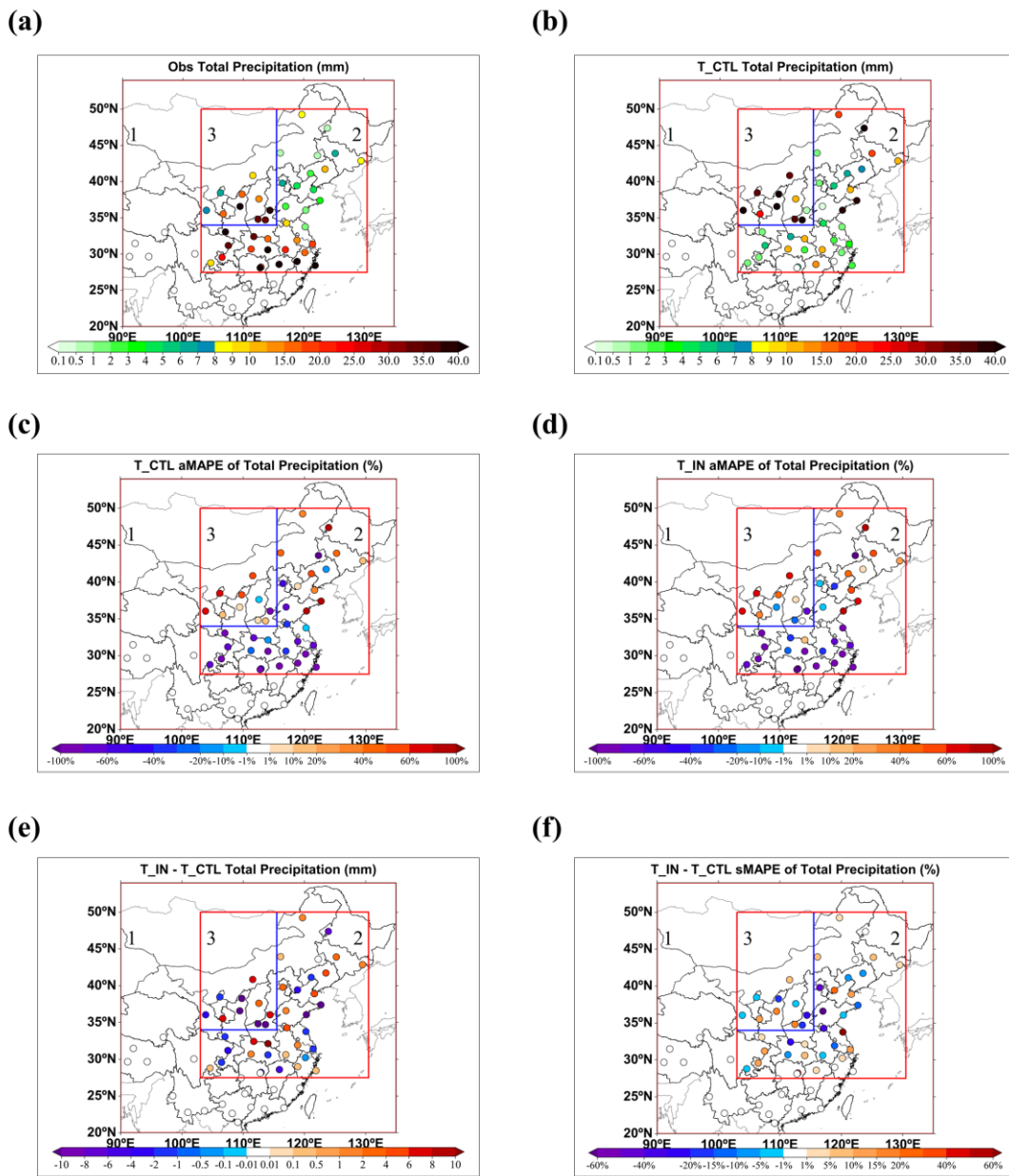


Figure 6. Comparison of observed and simulated accumulated precipitation at dust-precipitation stations:

(a) Observed accumulated precipitation from 11th 00:00 UTC to 15th 00:00 UTC;

(b) Same as a but for T_CTL;

(c) aMAPE of simulated accumulated precipitation in T_CTL;

(d) aMAPE of simulated accumulated precipitation in T_IN;

(e) Difference in precipitation between T_IN and T_CTL;

(f) Difference in sMAPE between T_IN and T_CTL.

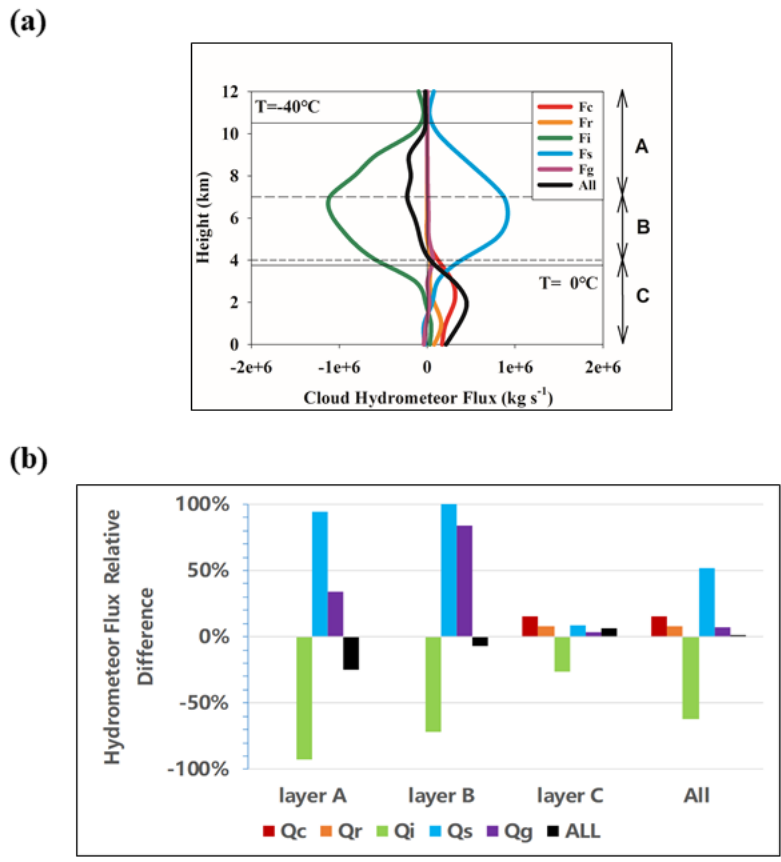


Figure 7. Horizontal hydrometeor fluxes across 116°E (33°–50°N) and 33°N (103°–116°E).

Here, Fc denotes cloud water flux, Fr rainwater flux, Fi cloud ice flux, Fs snow flux, Fg graupel flux, and All the total hydrometeor flux.

(a) Differences in horizontal hydrometeor fluxes ($T_{IN} - T_{CTL}$).

(b) Fractional changes in horizontal hydrometeor fluxes in Layers A, B, C, and the total column, defined as

$(T_{IN} - T_{CTL}) / T_{CTL}$. Snow and graupel fluxes in Layer A show extremely large increases (about 1883 % and 683 %, respectively); for better visualization, these values are scaled down by a factor of 20 in

the figure.

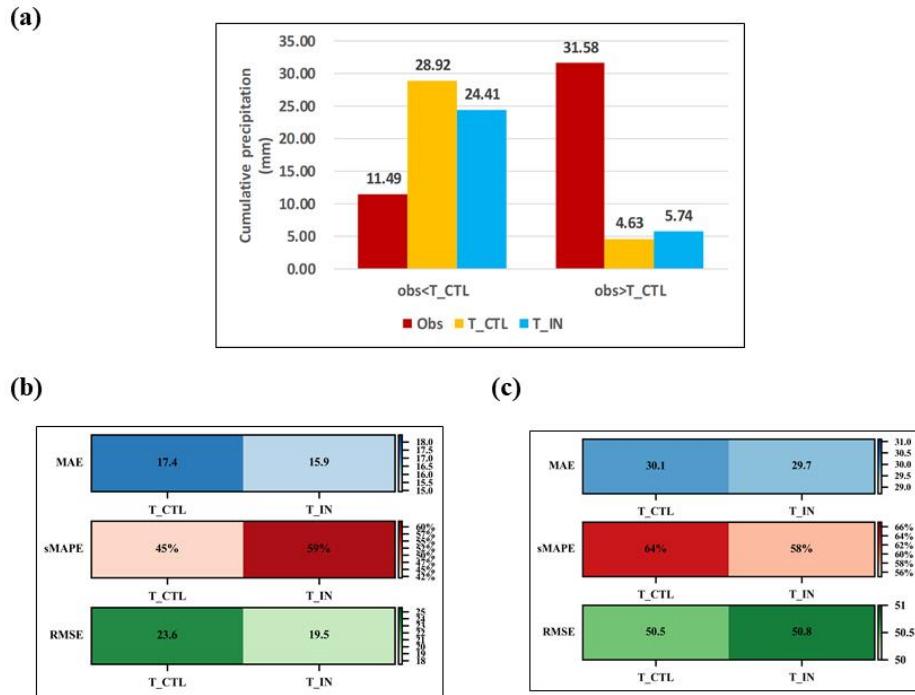


Figure 8.

(a) mean accumulated precipitation during DP event at overestimated stations and underestimated stations

(b) Statistical analysis of observed versus simulated accumulated precipitation at DPA stations for Overestimated stations

(c) same as (b), but for Underestimated stations

985 **Table**

Table 1. Tests designed for different types of microphysics scheme

Test	Warm cloud	Cold cloud
T_CTL	online aerosol–CCN interaction scheme	original WDM6
T_IN	online aerosol–CCN interaction scheme	online aerosol-IN nucleation scheme

986

987

988

Table 2. List of Symbols

Symbol	Meaning
Paacw	Production rate for accretion of cloud water by averaged snow/graupel (Under subfreezing conditions ($T < 0$ °C), the collected droplets are typically supercooled and freeze onto the surface of snow or graupel particles. In this case, cloud water is converted into snow or graupel, and latent heat of fusion is released, contributing to local warming. Under above-freezing conditions ($T > 0$ °C), the accreted droplets do not freeze.)
Pcact	Production rate for cloud droplet activation from CCN
Pcond	Production rate for condensation rate of water vapour to cloud liquid water
Pgacr	Production rate for accretion of rain by graupel
Pgaci	Production rate for accretion of cloud ice by graupel
Pgaut	Production rate for aggregation form snow to graupel
Piacr	Production rate for accretions of rain by cloud ice
Pidep	Production rate for deposition- sublimation rate of cloud ice
Pigen	Production rate for heterogeneous nucleation
Pinud	Production rate for deposition/condensation freezing to form cloud ice
Pinui	Production rate for immersion freezing of cloud water to form cloud ice
Pracs	Production rate for accretions of cloud snow by rain
Pracw	Production rate for accretion of cloud water by rain
Praci	Production rate for accretion of cloud ice by rain
Praut	Production rate for aggregation form cloud water ice to form rain

Prevps	Production rate for evaporation/condensation rate of cloud water
Prevp	Production rate for evaporation/condensation rate of rain
Psacr	Production rate for accretions of rain by cloud snow
Psaci	Production rate for accretion of cloud ice by snow
Psaut	Production rate for aggregation form cloud ice to snow
Pscar	Production rate for accretion of rain by snow
Psdep	Production rate for deposition- sublimation rate of cloud snow

989

